An Inverse Mean-Line Design Method for Optimizing Radial Outflow Two-phase Turbines in Geothermal Systems

Hongyang Li
E-mail: Hongyang.Li@glasgow.ac.uk
James Watt School of Engineering, University of Glasgow
Glasgow G12 8QQ, UK

Sham Rane
E-mail: sham.rane@eng.ox.ac.uk
Department of Engineering Science, University of Oxford
Oxford OX2 0ES

Zhibin Yu[1]

E-mail: Zhibin.Yu@glasgow.ac.uk
James Watt School of Engineering, University of Glasgow
Glasgow G12 8QQ, UK

Guopeng Yu
E-mail: Guopeng.Yu@glasgow.ac.uk
James Watt School of Engineering, University of Glasgow
Glasgow G12 8QQ, UK

Abstract

Radial outflow two-phase turbine (ROTPT) is an impulse two-phase turbine used for total flow systems in applications like geothermal fields to utilize the two-phase geofluid energy effectively. This paper presented a one-dimensional nonequilibrium inverse mean-line design method of ROTPT. With prescribed pressure and blade angle distributions, the averaged geometry and flow parameters in the rotating impeller channels were derived along the flow direction, the pressure distribution was formulated on the pressure side (PS) and the suction side (SS), and performance parameters were deduced in the implementation of the presented algorithm, including torque, output power, efficiency, etc. By using the design method, a ROTPT for a geothermal system was constructed. The flow field of the ROTPT was simulated in CFX using the thermal phase change model, which was validated by experimental results. By evaluating the averaged distribution and examining the three-dimensional flow, it was suggested that the presented design was consistent with the averaged flow in ROTPT. Meanwhile, there were three-dimensional effects in the rotating channel causing the deviation between the design and CFD results. This paper provides a nonequilibrium solver for designing ROTPTs but

[1] Corresponding author.

also can bolster the development of two-phase flow with the phase change in curved rotating channels.

Keywords: Total flow systems; Inverse design; Mean-line method; Flashing flow; Multiphase flow numerical simulation; Radial outflow two-phase turbine.

1 Introduction

Two-phase geofluid energy vastly exists and is under-utilized in many geothermal fields. Effective thermal to power conversion in these areas is of great significance for sustainable energy development. Based on the ‘total-flow’ concept, two-phase turbine (TPT) is expected to provide a more efficient and economically competitive solution for geothermal energy utilization. Analogously, it can increase the efficiency for many systems such as geothermal system[1], LNG system[2], refrigeration system[3], supercritical compressed-air energy system[4], etc.

The previous research on TPTs was mainly concentrated on the two-phase impulse turbine (TPIT) and the two-phase reaction turbine (TPRT). For TPITs, the entire depressurization process is inside the nozzle or the stator. The two-phase mixture flow issued from the nozzle drives the impeller to rotate and generate shaft power. Because the flow rate is generally limited in relevant systems, partial admission is adopted in TPITs frequently. Several researchers, including Starkman et al.[5], Brown[6], Neusen[7], and Maneely[8], compared the performance of different models including isentropic homogenous equilibrium (IHE) model, slip flow model and frozen composition model in predicting the critical flow rate of converging-diverging nozzles for the low quality steam. Austin et al.[1] took the Salton Sea geothermal area as the case and proposed a total flow system in which a TPIT converted the energy from the hot brine to the shaft power directly. With TPIT, the total flow system was with 60% better efficiency than the flashed system and binary cycle system[9]. Alger[10] studied the performance of nozzles used in TPIT for the total flow system and suggested IHE was a reasonably accurate tool for design and performance predictions. Comfort III el al.[11–13] studied the selection, the design method and the performance analysis of TPIT for the total flow system and the efficiency of the turbine was 23%. Elliott[14] presented comprehensive studies on the design method and experiment on the single-stage and the multi-stage TPIT with various working fluids. Hays et al.[15] described a one-dimensional code for designing an R134a TPIT. The maximum efficiency was 65%, but the stagnation loss limited the accuracy of the performance analysis method. Hays et al. [16] reported the TPIT used in a chiller system in Manhattan. The output power of the turbine was 54 kW, and the rotational speed was 1800 rpm. Brasz[17] stated that the ratio of the nozzle spouting velocity to the rotor speed affected the performance of a R134a TPIT significantly. Cho et a.[3] presented the design and experiment on a TPIT with supersonic nozzles for the chiller system. The maximum efficiency was 15.8% and the output power was 32.7 kW. He et al.[18] presented twin arc blade impeller for a Pelton type TPIT using R410a as the working fluid. Experimental results showed that the peak efficiency was 32.8% and the maximum rotational speed was 26500 rpm. Beucher et al.[19] studied the friction loss formula for the Pelton type TPIT through experiment and CFD. Araj et al.[20] presented another Pelton type TPIT with 5 nozzles and 24 buckets with finite element method (FEM). Hays and Elliott[21] proposed the patent for two-phase engine used in vehicles. Studhalter et al.[22] reported the Biophase TPIT used in a geothermal system could increase 20% output power compared with the single flash TPIT.

For TPRTs, there are two configurations based on the structure of the turbine studied in the previous literature, including the radial inflow two-phase turbine (RITPT) and the radial outflow two-phase turbine (ROTPT). For RITPTs, Zhang et al.[23] constructed a prototype with six stators and eleven rotors using R22 as the working fluid in the subcritical refrigeration system. The efficiency of the turbine was 10.4% and the rotational speed was 3200 rpm. Traditional design methods and parameters of radial inflow turbines for pure gas or pure liquid are not suitable for RITPT.

For ROTPTs, they are also called as the Hero's turbine or the pure reaction two-phase turbine in previous studies. Akagawa et al.[24] tested a ROTPT with three channels in a 200 mm impeller diameter and found that the loss of the two-phase flow channel was larger than the single-phase flow. Akagawa et al.[25] and Ohta et al.[26] carried out experimental investigation and the performance analysis on the nozzle which could work as the channel used in ROTPTs. Fujii et al.[27] developed an expression of internal efficiency of the ROTOT used in the total flow system. Zhao et al.[28] and Date el al.[29] designed and tested ROTPTs used in the solar power system based on the patent proposed by Fabris[30]. A two-step method was put forward for designing the channel based on IHE model and experimental results. The turbine efficiency was 25% under the condition of the maximum output power. Rane et al.[31–34] validated mathematical models on BNL nozzle[35,36] and ROTPT[28] through comparison between CFD and experimental results. Optimal model and model parameters were obtained for ROTPTs in CFX software. Compared to TPITs, the impeller of ROTPT has advantages of simple structure and moderate cost. Based on the previous studies on two-phase flow in stationary nozzles[37–39], single-phase flow in rotating channels[40] and multiphase flow models with CFD[31,41], ROTPT has a great prospect of applications in the energy recovery and geothermal systems.

Mathematical models describing the vaporization mainly include analysis model for turbomahcinery[42,43], evaporation-condensation model[44], cavitation model[45,46], wall boiling model[47], flashing model[48,49] and so on. Karathanassis et al.[50] simulated the flashing flow in the Moby Dick nozzle using both the cavitation model and the flashing model, and stated that the cavitation and the flashing are of different nature. Because driving forces of the vaporization in ROTPT are mainly the depressurization of the fluid and the heat transfer between two phases, the flashing model is suitable to describe the formation and the development of the vapour in the channels of ROTPT.

Previous numerical studies on the flashing flow in convergent-divergent nozzles have introduced various reliable numerical models. Le et al.[51] compared the numerical simulation using ad hoc modelling of the boiling delay with experimental results of BNL nozzles. Angielczyk et al.[52] presented the enhanced Possible-Impossible Flow algorithm to predict the flashing flow of CO_2 in the two-phase ejector and found that the conventional Delayed Equilibrium Model (DEM) for water is not suitable for the flashing of CO_2. Gärtner et al.[53] used the one-fluid approach and the homogeneous relaxation model to study the flashing flow of cryogenic nitrogen. Zhu et al.[54,55] employed the thermal phase change model in the simulation of the enhanced flashing flow of R134a with the vortex generator applied and validated simulation results with the experiment. Yin et al.[56] compared different mathematical methods for the nucleation and flashing inception and found that the pressure undershoot was affected by nucleation rates and heterogeneity factors. Liao et al.[57] reviewed previous numerical models for generally simulating the flashing flows and pointed out that closure models were of high influence on the accuracy of the prediction, including interphase transfer, bubble dynamics (nucleation, coalescence and breakup) as well two-phase turbulence.

For a ROTPT's impeller, the inlet and outlet flow parameters are highly correlated with the flow along a channel. Lacking published correlations or experimental data in rotating two-phase flow channels has imposed considerable difficulties in building efficient design models for ROTPT's channels. The direct three-dimensional design method using CFD technology can consume huge computing resources and requires long and costly design cycles. Therefore, it is essential to develop a reliable indirect one-dimensional inverse mean-line design method for ROTPT prior to numerical investigations.

In this paper, subcooled liquid at the inlet vaporizes in the rotating channel of ROTPT. By using the presented inverse design method, geometrical and flow parameters of the channel can be derived under given pressure distribution and blade angle distribution inversely.

2 Design Method

2.1 Impeller Geometry and Velocity Triangles

The flow in the impeller is shown in Figure 1(a). High-pressure subcooled liquid flows into the impeller in the axial direction and is fed into different channels of the impeller. The pressure of the flow decreases gradually along the channel, and the liquid vaporizes in the channel. Finally, the mixture of the liquid and the vapour leaves the channel. The impeller includes three segments: the inlet tube (IT), the inlet section (IS) and the main flow passage (MFP), as shown in Figure 1(b). IT collects the subcooled liquid from the inlet pipe. IS and MFT are the two sections of the rotating channel. IS connects IT and MFP. The shape of MFP, as shown in Figure 1(c), can control the depressurization and vaporization process.

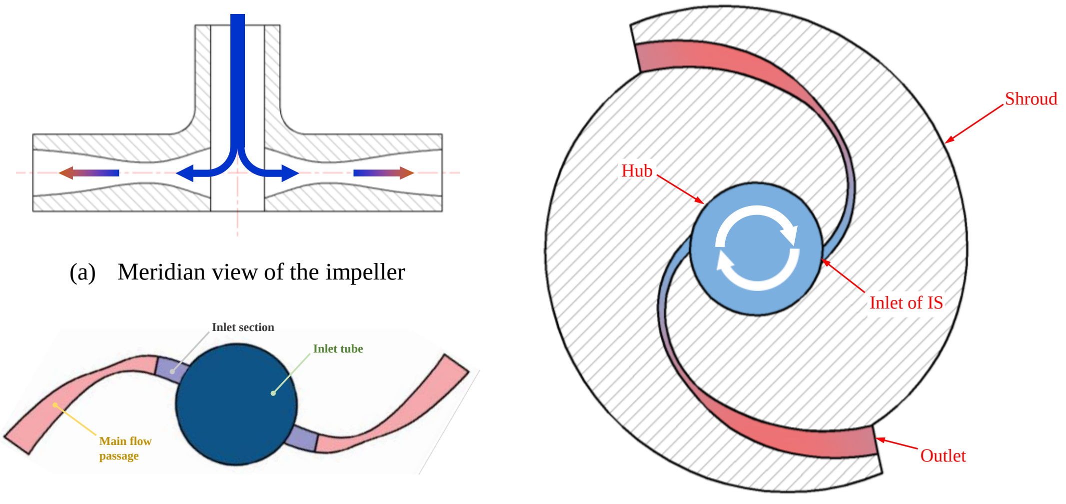

(a) Meridian view of the impeller

(b) Sections of the channel

(c) Cross-section of the channel

Figure 1. Diagram of the channel in TPROT

Parameters of the rotating channel can be categorized into two types, including the geometrical parameters and the flow parameters as shown in Table 1. Geometrical parameters are related with geometry information of the channel. Flow parameters contain state and process parameters of the fluid in the channel.

Table 1 Parameters in the channel

Geometrical parameters	Flow parameters
Position	Pressure
Polar angle	Temperature
Blade angle	Relative velocity
Width	Absolute velocity

Height	Relative flow angle
Curvature radius	Absolute flow angle
Length	
	…

The MFP is enclosed by six surfaces, as shown in Figure 2(a), which include Pressure Side (PS), Suction Side (SS), Top Side (TS), Bottom Side (BS), Inlet and Outlet. The inlet of the MFP is connected to the outlet of IS and the outlet of MFP is the outlet of the channel. The cross-section of MFP is square along the flow direction, as shown in Figure 2(b). It can be noted that the shape of the centerline and the area A of the channel along the flow direction L are crucially important to the design of the rotating channel. The centerline of MFP is illustrated as the red dot-dash line in Figure 1(b) and affects the bending of the channel.

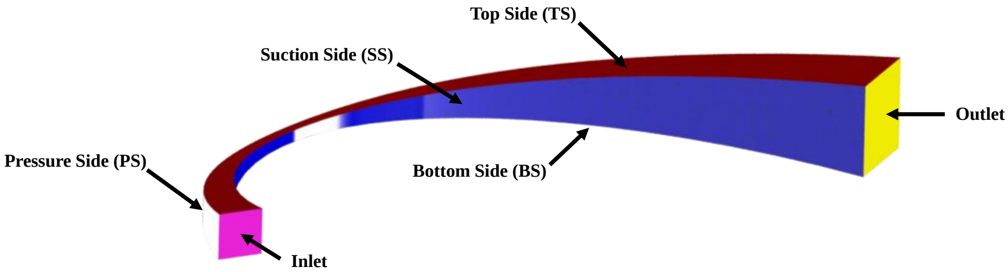

(a) Boundary surfaces of MFP

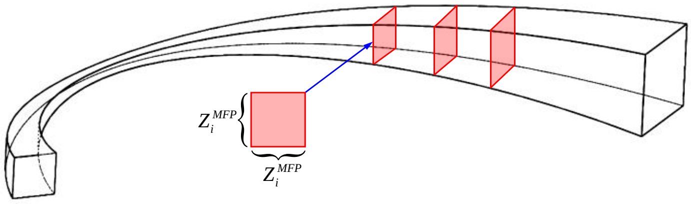

(b) Cross-sections of MFP

Figure 2. Diagram of MFP

Three target curves should be designed precisely, including the centerline (CL), the pressure line (PL) and the suction line (SL) on the two-dimensional middle cross-section plane, as shown in Figure 3. PL and SL are dependent on the shape of CL and the distribution of the area along the flow direction.

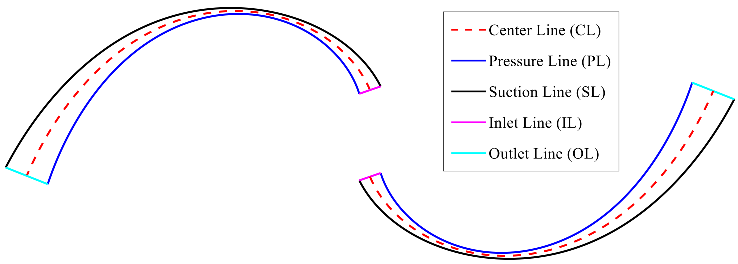

Figure 3. Target curves of MFP

The output power of the impeller is obtained from the thermal fluid. Flow in the channel accelerates due to the change of the internal energy and drives the impeller to output power. The inlet and the outlet velocity triangle are shown in Figure 4. The velocity triangles of ROTPT are different from radial inflow or axial turbines. The flow in ROTPT accelerates remarkably due to the vaporization. The acceleration is useful to convert the fluid energy to the shaft power.

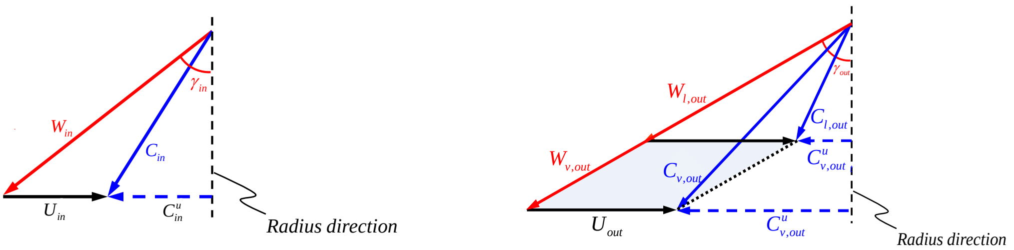

(a) Inlet (b) Outlet

Figure 4. Velocity triangles at inlet and outlet

2.2 Mathematical Models of Geometry

For designing the cross-sectional area of a rotating channel, mathematical models are built according to geometrical relationships and physical laws. For a point Q on CL, which represents an element in the channel, as shown in Figure 5, two different coordinate systems can be established. One is the stationary coordinate system Π^s based on the rotating center of the impeller. The other is the coordinate system Π^c based on the movable point Q of CL. Coordinate axes on Π^c are in the direction s_i^t and the direction s_i^n. The direction s_i^t is the flow direction, and the direction s_i^n is perpendicular to the flow direction on the x-y plane. For convenience, the z direction is called the spanwise direction.

The polar angle $\theta(x, y)$ of the point $Q(x, y)$ on Π^s between the radial direction and the x-axis is calculated as

$$\tan\theta = \frac{y}{x} \tag{1}$$

The blade angle $\beta(x, y)$ between the flow direction s_i^t and the x-axis represents the slop of the centerline at the point $Q(x, y)$ and can be calculated through Equations (2) and (3)

$$\Delta y = \Delta L \sin\beta \tag{2}$$

$$\Delta x = \Delta L \cos\beta \tag{3}$$

The relative flow angle γ represents the deviation between the flow direction s_i^t and the radial direction s_i^n, which can be calculated as

$$\gamma = \theta - \beta \tag{4}$$

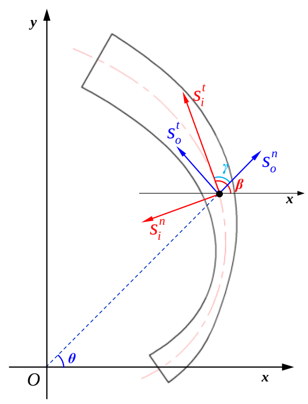

Figure 5. Directions and angles for a point on CL

2.3 Physical Laws

Based on the conservation of mass, momentum and energy, mathematical models can be built on the element i in the rotating channel, as shown in Figure 6. There is no mass flow across TS, BS, PS and SS, as shown in Figure 6(a). Several assumptions must be made, including:

1. Flow parameters and thermal properties are averaged within the element.

2. Directions of the relative liquid velocity W_l and the relative vapour velocity W_v are the identical, i.e. $\gamma_v = \gamma_l$, as shown in Figure 4(b).
3. The minimum vapour fraction $\alpha_{\min}$ is 1.0^{-6}.
4. The minimum mean bubble diameter D_b is 1.0^{-5} m.
5. The bubble number density N_b is 5.0×10^{7}.
6. The temperature of the vapour T_v is the saturation temperature under the local pressure.
7. The pressure on TS and BS is equivalent to the pressure at the center point.

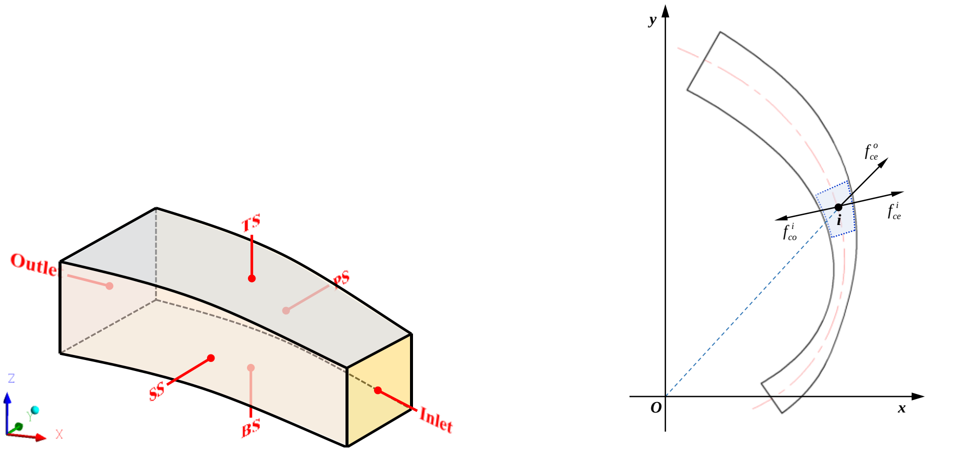

(a) Surfaces of the element *i* (b) Body force of the element *i*

Figure 6. Diagram of the element *i* in the channel

2.3.1 Conservation of mass, momentum, and energy

Based on the conservation of mass, Equation (5) can be derived

$$\frac{d\left[\alpha A\rho_v W_v + (1-\alpha)A\rho_l W_l\right]}{dL} = 0 \tag{5}$$

On the inlet or outlet plane of the element shown in Figure 7(b), Equation (5) can be rewritten in the following form

$$\alpha A\rho_v W_v + (1-\alpha)A\rho_l W_l = m \tag{6}$$

And the average density ρ_m is $\alpha\rho_v + (1-\alpha)\rho_l$. Based on the conservation of momentum, Equation (7) can be derived in the flow direction

$$\frac{d\left[\alpha A\rho_v W_v^2 + (1-\alpha)A\rho_l W_l^2\right]}{dL} = -A\frac{dP}{dL} - A\left(\frac{dP}{dL}\right)_f + A\left[\alpha\rho_v + (1-\alpha)\rho_l\right] f_{ce}^{o}\cos\gamma \tag{7}$$

where $f_{ce}^{0} = \Omega^2 r$. Based on the conservation of energy, Equation (8) can be derived as

$$\frac{d\left[\alpha A\rho_v W_v\left(H_v + \frac{W_v^2 - U^2}{2}\right) + (1-\alpha)A\rho_l W_l\left(H_l + \frac{W_l^2 - U^2}{2}\right)\right]}{dL} = -\frac{dPo_f}{dL} \tag{8}$$

where Po_f is the energy loss due to the friction and can be evaluated by

$$\frac{dPo_f}{dL} = A\left(\frac{dP}{dL}\right)_f dL \tag{9}$$

2.3.2 Vapour generation model

Due to the phase change, there is a mass transfer between the liquid and the vapour. Thus, Equation (10) can be derived as

$$\frac{d\left[\left(1-\alpha\right)A\rho_l W_l\right]}{dL}=-\frac{dm_{lv}}{dL} \tag{10}$$

where the right item in Equation (10) is the mass source.

The thermal flow change model is used to calculate the mass source. Thus, the interphase mass flow rate is read as

$$\frac{dm_{lv}}{dL}=\frac{h_{lv}A_{\text{int}}\left(T_l-T_v\right)A}{H_l-H_v} \tag{11}$$

Wolfert model[58] is used to evaluate the heat transfer coefficient. Peclet number Pe is

$$Pe=\frac{D_b\left|C_v-C_l\right|}{\chi} \tag{12}$$

where χ is the thermal diffusivity. Jakob number Ja is

$$Ja=\frac{\rho_l Cp_l T_{\text{sup}}}{\rho_v\left(H_l-H_v+1.0^{-12}\right)} \tag{13}$$

where T_{sup} is the super heat of the liquid and calculated as

$$T_{\text{sup}}=\max\left(T_l-T_v,0\right) \tag{14}$$

The Nusselt number Nu_{lv} is

$$Nu_{lv}=\frac{12Ja}{\pi}+2\sqrt{\frac{Pe}{\pi}} \tag{15}$$

Thus, the heat transfer coefficient h_{lv} between the liquid and the vapour is

$$h_{lv}=\frac{Nu_{lv}K_l}{D_b} \tag{16}$$

The interfacial area A_{int} between the liquid and the vapour is

$$A_{\text{int}}=\frac{6\alpha}{D_b} \tag{17}$$

The vapour mass fraction x_v can be deduced from Equation (18)

$$\frac{dx_v}{dL}=\frac{1}{m}\frac{dm_{lv}}{dL} \tag{18}$$

2.3.3 Slip model and frictional pressure reduction model

The slip between the liquid and the vapour can be modelled with a vapour sphere particle. In Equation (19), the momentum conservation law is applied on the particle, where C_D is the drag coefficient. The slip ratio S can be derived by solving this equation.

$$\frac{\pi D_b^3}{6}\rho_v W_v\frac{\mathrm{d}W_v}{\mathrm{d}L}=-\frac{\pi D_b^2}{4}\frac{dP}{dL/D}+\frac{\pi D_b^3}{6}\rho_v\Omega^2 r\cos\gamma-\frac{\pi D_b^2}{8}C_D\left(W_v-W_l\right)\left|W_v-W_l\right| \tag{19}$$

The void fraction α can be evaluated using Equation (20).

$$\alpha=\frac{x_v\rho_l}{\left(1-x_v\right)\rho_v S+x_v\rho_l} \tag{20}$$

The correlation of the frictional pressure reduction $(dP/dL)_f$ was firstly proposed by Lockhart and Martinelli[59]. Although the correlation has been developed by many researchers[39], the appropriate correlation for rotating channels is few in the published literature. The correlation of [60] is used in the paper since it is suitable for single component. Reynold numbers of the liquid and the vapour are

$$\mathrm{Re}_l = \frac{m}{A}\frac{Z}{\upsilon_l} \tag{21}$$

$$\mathrm{Re}_v = \frac{m}{A}\frac{Z}{\upsilon_v} \tag{22}$$

The friction coefficient for only liquid f_{lo} is

$$f_{lo} = 0.25\left[\lg\left(\frac{150.39}{\mathrm{Re}_l^{0.98865}} - \frac{152.66}{\mathrm{Re}_l}\right)\right]^{-2} \tag{23}$$

The friction coefficient for only vapour f_{vo} is

$$f_{vo} = 0.25\left[\lg\left(\frac{150.39}{\mathrm{Re}_v^{0.98865}} - \frac{152.66}{\mathrm{Re}_v}\right)\right]^{-2} \tag{24}$$

The frictional pressure reduction for only liquid is

$$\left(\frac{dP}{dL}\right)_{f,lo} = \frac{f_{lo} m^2}{2A^2 \rho_l Z} \tag{25}$$

The frictional pressure reduction for only vapour is

$$\left(\frac{dP}{dL}\right)_{f,vo} = \frac{f_{vo} m^2}{2A^2 \rho_v Z} \tag{26}$$

The factor of two-phase frictional pressure reduction Φ is

$$\Phi = \left(1 + 0.54 La\sqrt{1 - x_v}\right)\left\{Y^2 x_v^3 + \left(1 - x_v\right)^{0.33}\left[1 + 2x_v\left(Y^2 - 1\right)\right]\right\} \tag{27}$$

where Y and La is

$$Y = \sqrt{\left(\frac{dP}{dL}\right)_{f,lo} \Big/ \left(\frac{dP}{dL}\right)_{f,vo}} \tag{28}$$

$$La = \sqrt{\frac{\sigma}{9.807\left(\rho_l - \rho_v\right)WD}} \tag{29}$$

Thus, the pressure reduction due to friction in two-phase flows is

$$\left(\frac{dP}{dL}\right)_f = \Phi\left(\frac{dP}{dL}\right)_{f,lo} \tag{30}$$

Using Equations (5), (6), (7), (8), (10), (19), (20) and (30), all mathematical equations are closed, and all parameters can be solved using an appropriate algorithm.

2.4 Solver

According to the mathematical equations mentioned above, when the distributions of the pressure and the blade angle are given, as well as sufficient design parameters, the shape of the channel can be determined using an inverse solver. The presented solve uses the one-order upwind scheme, which is fast and robust, although high-order schemes may derive higher accurate results.

2.4.1 The frame of the solver

To solve the above equations by the numerical method, MFP is divided uniformly along the flow direction as shown in Figure 7. The total length of the channel L is $\tau_l r_1$ and the space interval ΔL is $L/(n-1)$. All parameters are solved at computational station i using finite volume method (FVM). For node i+1/2, a parameter ϕ is calculated using Equation (31).

$$\phi_{i+1/2} = \phi_i + \phi_{i+1} \tag{31}$$

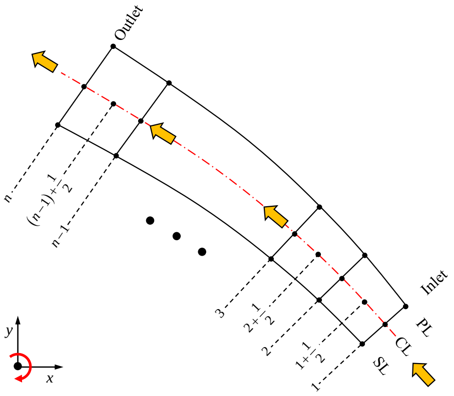

Figure 7. Computational stations in MFP

The whole design algorithm consists of four programs, including CL design, MFP cross-sectional area design, IS design and output power evaluation, as illustrated in Figure 8. The procedure of the whole design method is illustrated in Appendix A.

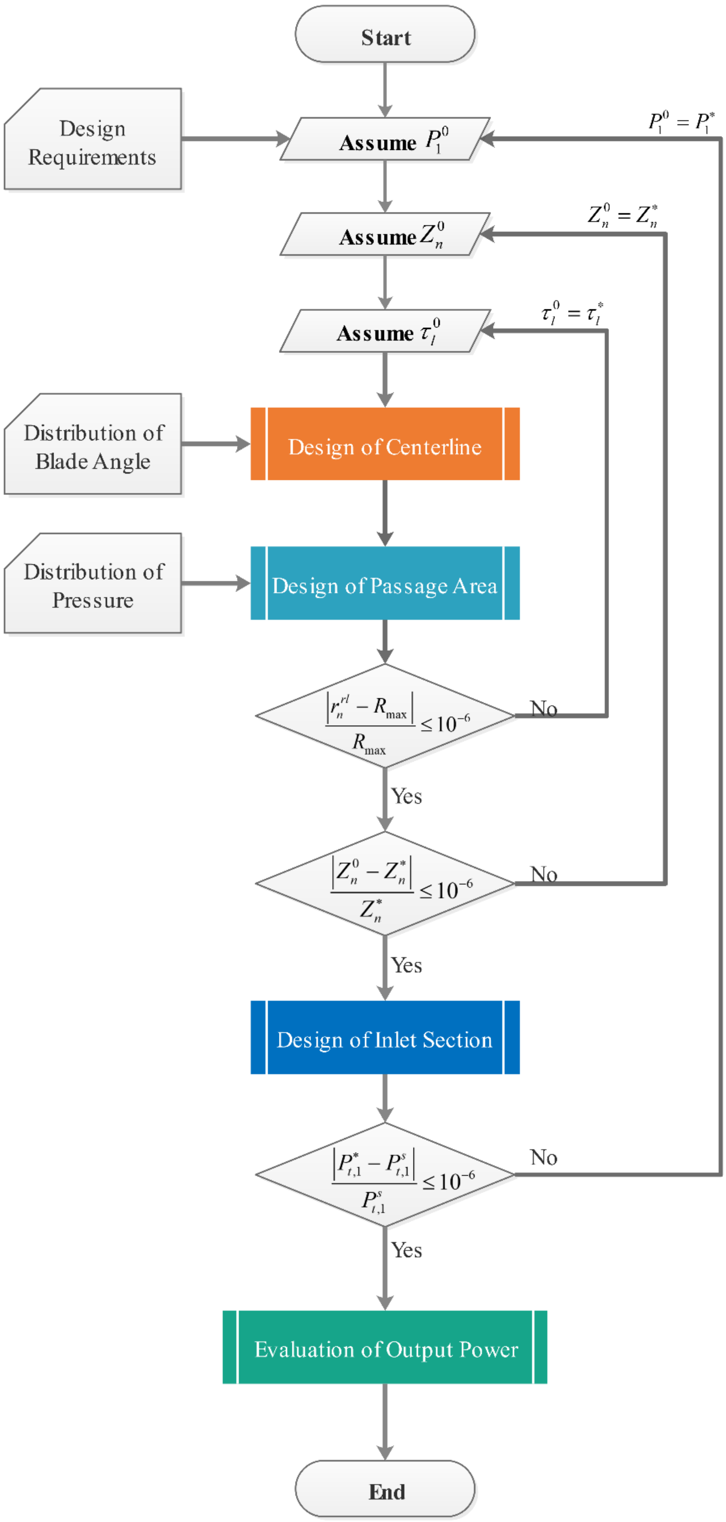

Figure 8. The design process of the channel

The corrected values are given according to the results of the three design programs. According to Equation (6), the corrected width $Z^*_{n_{mfp}}$ is

$$Z^*_{n_{mfp}} = \tau_z \sqrt{\frac{m/B_N}{\alpha_{n_{mfp}} W_{v,n_{mfp}} \rho_{v,n_{mfp}} + \left(1-\alpha_{n_{mfp}}\right) W_{l,n_{mfp}} \rho_{l,n_{mfp}}}} \tag{32}$$

where τ_z is the width factor. The corrected length ratio τ_l^* is

$$\tau_l^* = \frac{r_n^{pl}}{R_{\max}} \tau_l^0 \tag{33}$$

where $R_{\max}$ is the set value of the maximum radius of MFP according to the design requirements. The corrected pressure P_1^* is

$$P_1^* = P_1^0 + \left(P_0^{t,s} - P_0^t\right) \tag{34}$$

where $P_0^{t,s}$ is the set value of the inlet total pressure according to design requirements.

2.4.2 Design of MFP's CL

The procedure of the program of designing CL of MFP is shown in Figure 9 and Appendix B. When the position of the first node is given, positions of other nodes can be derived. Other ways for deriving CL can also be adopted. For example, in this paper the distribution of the flow angle is the given condition, and the distribution of the blade angle is the derived result. In some cases, it is more convenient if the distribution of the blade angle is the given condition, and the distribution of the flow angle is the derived result. However, it is hard to adjust the distribution of the blade angle to get a smooth enough distribution of the flow angle. So, in this paper, a smooth distribution of the flow angle is given, and the distribution of the blade angle is the derived result.

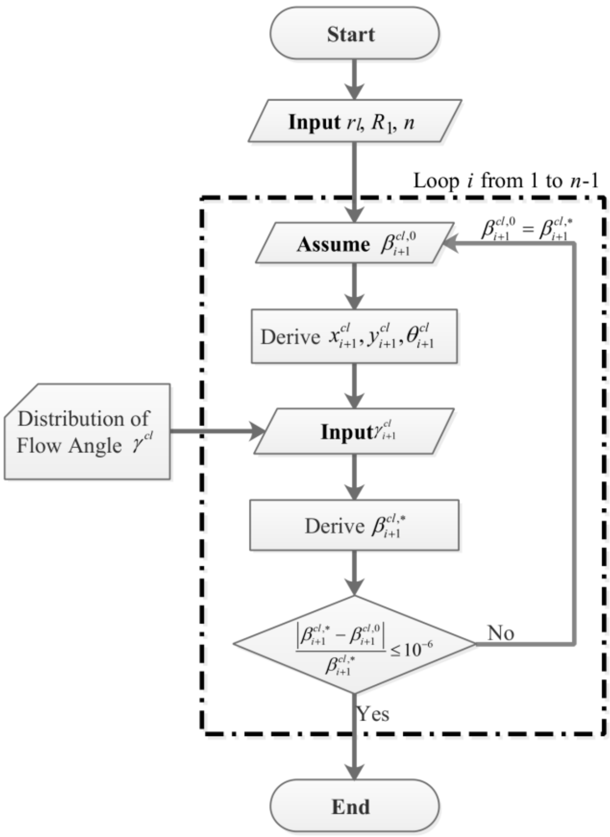

Figure 9. Algorithm for designing CL

The distribution of the relative flow angle γ^{cl}, the inlet relative flow angle γ_{in}^{cl} and the outlet relative flow angle γ_{out}^{cl} affect the CL significantly, as shown in Figure 10. Under the same inlet relative flow angle, the CL with the low outlet relative flow angle has a short length. Under the same outlet relative flow angle, the CL of the low inlet relative flow angle has a more distinct bending.

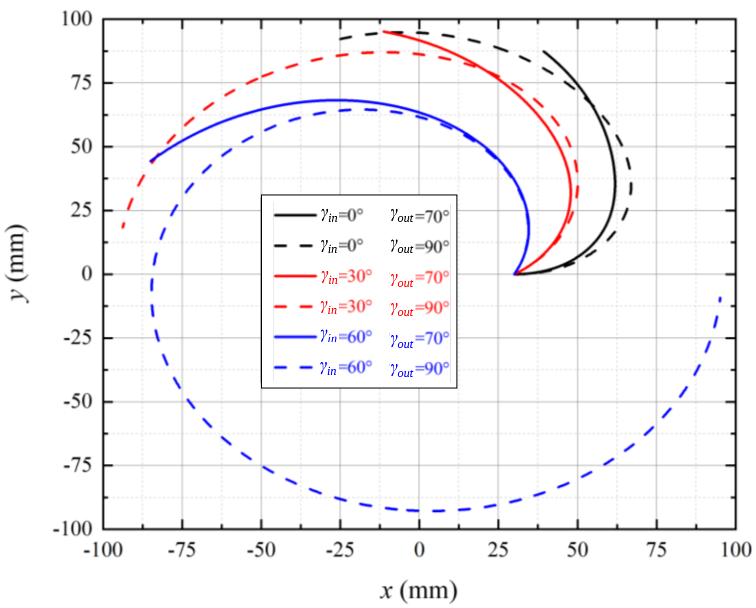

Figure 10. Centerlines of MFP under different γ_{in} and γ_{out}

2.4.3 Design of MFP's cross-sectional area

The procedure of the design of MFP's area is shown in Figure 11 and Appendix C. The distribution of pressure should be given along CL. Because the pressure undershoot is of great importance in flashing nozzles, there is a large gradient of pressure in the distribution. Thermal properties of the vapour are assumed to be identical with the saturation properties at the local pressure. There are four lays of iteration for solving the void fraction, the area, the slip ratio and the liquid temperature sequentially. Other orders of the layers may also be applied in this program. But this order is highly recommended because it is robust for most cases.

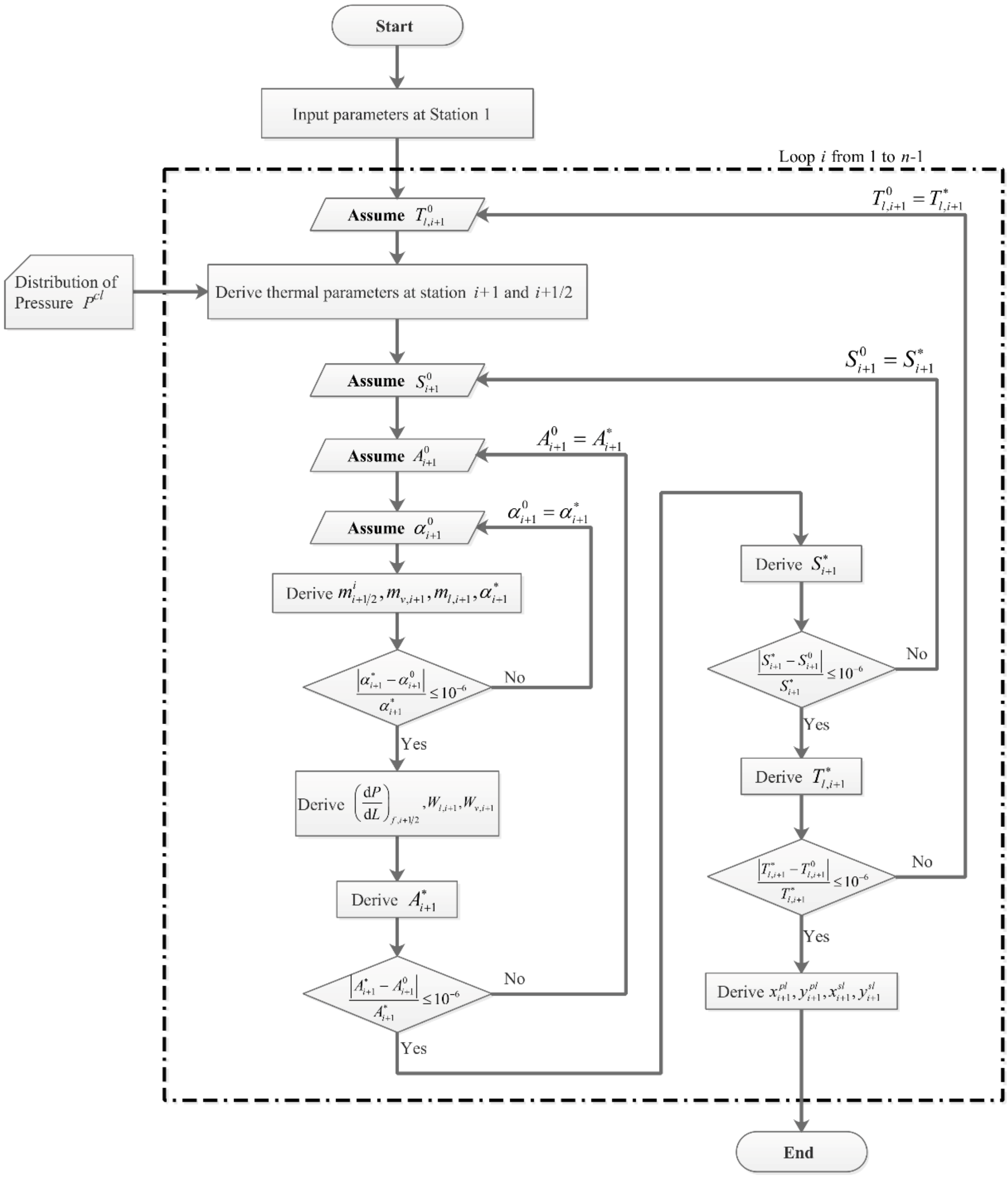

Figure 11. Algorithm for designing the area of MFP

2.4.4 Design of IS

IS connects IT and MFT and guides the subcooled liquid to flow from IT to MFT, as shown in Figure 12(a) and (b). Different shapes of IS also affect the performance of the impeller. But, to build IS as simple as possible, PL and SL of IS are straight lines which are tangent to PL and SL of MFP separately in this paper. After attaining the design of MFP's CL and MFP's area, PL, SL, inlet, and outlet of MFP are obtained. The outlet of IS has been exposed since it is the same to the outlet of IS, as shown in Figure 12(a). The cross section of IS is rectangular rather than square. But the height of IS at each computational stations is set to be the same to the inlet width of MFP for convenience, i.e. $h_i^{IS} = Z_1^{MFP}$ as shown in Figure 12(c).

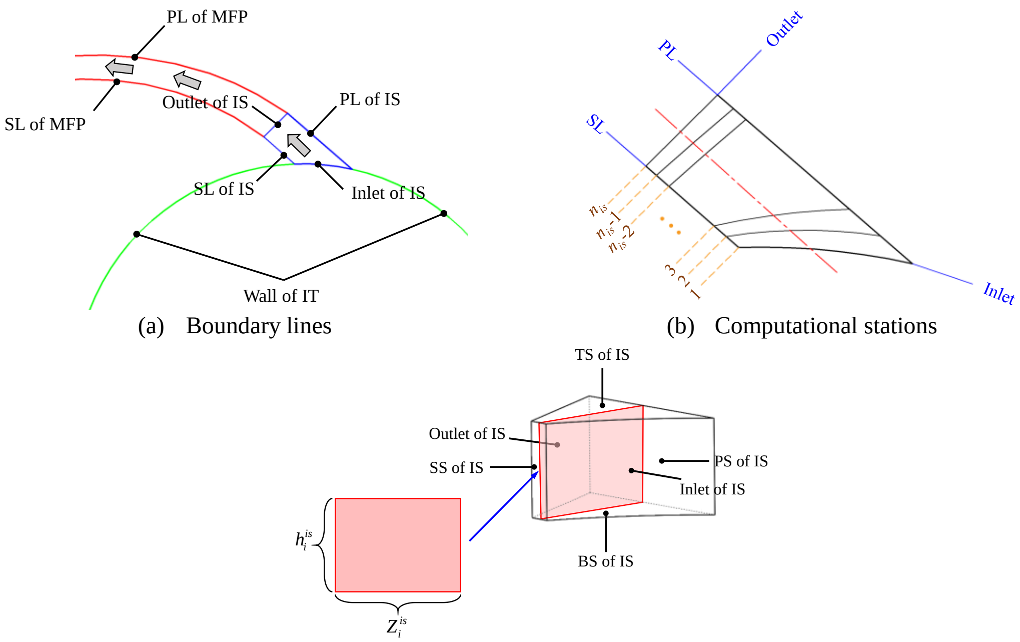

(a) Boundary lines (b) Computational stations

(c) Cross section

Figure 12. Diagram of IS

The blade angle of PL of IS is the same to the blade angle of PL of MFP at the inlet of MFP, i.e. $\beta_i^{pl,is} = \beta_1^{pl,mfp}$, while the blade angle of SL of IS is the same to the blade angle of SL of MFP at the inlet of MFP, i.e. $\beta_i^{sl,is} = \beta_1^{sl,mfp}$. The inlet of IS is determined by the inlet radius of IS R_{in}^{is}, which is decided according to the requirements of the structure. Positions of the first node are solved through Equation (35).

$$\begin{cases} \left(x_1^{pl}\right)^2 + \left(y_1^{pl}\right)^2 = R_{IT}^2 \\ \dfrac{y_1^{pl,is} - y_1^{pl,mfp}}{x_1^{pl,is} - x_1^{pl,mfp}} = \tan\beta_1^{pl,mfp} \\ \left(x_1^{sl}\right)^2 + \left(y_1^{sl}\right)^2 = R_{IT}^2 \\ \dfrac{y_1^{sl,is} - y_1^{sl,mfp}}{x_1^{sl,is} - x_1^{sl,mfp}} = \tan\beta_1^{sl,mfp} \end{cases} \tag{35}$$

Computational stations in IS are specified similarly to those in MFP, as shown in Figure 13(b). Computational stations of PL and SL are linearly distributed between the inlet and the outlet. For the computational station i, geometry parameters of PL, SL and CL can be derived by Equation (36).

$$\begin{cases} x_i^{pl,is} = x_1^{pl,is} + i\left(x_{n_{is}}^{pl,is} - x_1^{pl,is}\right)\Big/\left(n_{is}-1\right) \\ y_i^{pl,is} = y_1^{pl,is} + i\left(y_{n_{is}}^{pl,is} - y_1^{pl,is}\right)\Big/\left(n_{is}-1\right) \\ x_i^{sl,is} = x_1^{sl,is} + i\left(x_{n_{is}}^{sl,is} - x_1^{sl,is}\right)\Big/\left(n_{is}-1\right) \\ y_i^{sl,is} = y_1^{sl,is} + i\left(y_{n_{is}}^{sl,is} - y_1^{sl,is}\right)\Big/\left(n_{is}-1\right) \\ x_i^{cl,is} = \left(x_i^{pl,is} + x_i^{sl,is}\right)\Big/2 \\ y_i^{cl,is} = \left(y_i^{pl,is} + y_i^{sl,is}\right)\Big/2 \end{cases} \tag{36}$$

The polar angle and the flow angle of CL in IS can be calculated with Equation (37)

$$\begin{cases} \theta_i^{cl,is} = \arctan\left(y_i^{cl,is}/x_i^{cl,is}\right) \\ \gamma_i^{cl,is} = \beta_i^{cl,is} - \theta_i^{cl,is} \end{cases} \tag{37}$$

The width of IS is

$$Z_i^{is} = \sqrt{\left(x_i^{pl,is} - x_i^{sl,is}\right)^2 + \left(y_i^{pl,is} - y_i^{sl,is}\right)^2} \tag{38}$$

Because the vaporization happens in MFP, it can be assumed that several thermal properties in IS are constant and equal to the thermal properties at the inlet of MFP, for example the density, i.e. $\rho_{l,i}^{is} = \rho_{l,1}^{mfp}$. According to the conservation of mass, the relative flow velocity $W_{l,i}^{is}$ is

$$W_{l,i}^{is} = \frac{m\tau_z^2}{\rho_{l,i}^{is} Z_i^{is} h_i^{is}} \tag{39}$$

The Bernoulli equation in the relative frame is applied to determine the pressure in IS. The pressure along CL of IS is

$$P_i^{cl,is} = P_1^{cl,mfp} + \rho_{l,1}^{mfp}\left[\frac{\left(W_{l,1}^{mfp}\right)^2 - \left(U_1^{cl,MFP}\right)^2}{2}\right] - \rho_{l,i}^{is}\left[\frac{\left(W_{l,1}^{is}\right)^2 - \left(U_i^{cl,is}\right)^2}{2}\right] \tag{40}$$

2.4.5 Evaluation of output power

The output power of the impeller *Po* is generated by the force exerted by the flow in the rotating channel. Boundaries of an element in the channel are shown in Figure 13(a). The force on the element is shown in Figure 13(b). Each force is normal to the boundary except for the friction force.

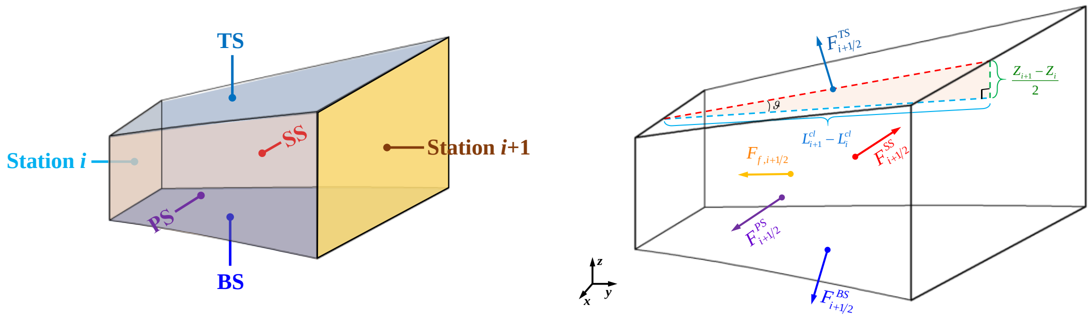

(a) Surfaces of an element (b) Forces on boundaries

Figure 13. Diagram of an element in the channel

The torque of the element $To_{z,i+1/2}$ and the output power Po is derived as Equation (41) and (43).

$$\begin{aligned} To_{z,i+1/2} = {} & F_{x,i+1/2}^{PS} y_{i+1/2}^{pl} - F_{y,i+1/2}^{PS} x_{i+1/2}^{pl} + F_{x,i+1/2}^{SS} y_{i+1/2}^{sl} - F_{y,i+1/2}^{SS} x_{i+1/2}^{sl} + F_{x,i+1/2}^{TS} y_{i+1/2}^{cl} \\ & - F_{y,i+1/2}^{TS} x_{i+1/2}^{cl} + F_{x,i+1/2}^{BS} y_{i+1/2}^{cl} - F_{y,i+1/2}^{SS} x_{i+1/2}^{cl} + F_{f,x,i+1/2} y_{i+1/2}^{cl} - F_{f,y,i+1/2} x_{i+1/2}^{cl} \end{aligned} \tag{41}$$

It should be noticed that the torque at the outlet of MFP should be deducted. The torque at the outlet can be simply calculated by

$$To_{out} = \iint_{A_{out}} r_{out}(x,y)\sin\left|\gamma(x,y)\right| P_{out} \mathrm{d}A(x,y) \tag{42}$$

Actually, T_{out} should be replaced with the torque generated on the hub and the shroud of the impeller as shown by Figure 1(c). Equation (42) only considers the force generated by the pressure without the friction. The evaluation of the friction torque requires geometry information of the shroud, which may be generated or constrained by the strength of the material and the structure of the turbine. For the design of the flow channel in this paper, the friction torque generated on the hub and the shroud is neglected.

$$Po = -\left(\sum_{i=1}^{n_{is}-1} B_N To_{z,i+1/2}\Omega + \sum_{i=1}^{n_{mfp}-1} B_N To_{z,i+1/2}\Omega - B_N To_{out}\Omega \right) \tag{43}$$

where B_N is the number of blades. The sign of Equation (43) is negative because for the case studied in this paper, the direction of the rotation is opposite to the z-axis, as shown in Figure 7. The first item in the right side of Equation (43) is termed as Po_{IS}, the second item in the right side of Equation (43) is termed as Po_{MFP}, and the third item in the right side of Equation (43) is termed as Po_{out}. In the design method, the friction force $F_{f,i+1/2}$ is simplified as Equation (44).

$$\begin{cases} F_{f,x,i+1/2} = -\left(\dfrac{dP}{dL}\right)_{f,i+1/2} \left(L_{i+1} - L_i\right) A_{i+1/2} \cos\left(\beta_{i+1/2} - \dfrac{\pi}{2}\right) \\ F_{f,y,i+1/2} = -\left(\dfrac{dP}{dL}\right)_{f,i+1/2} \left(L_{i+1} - L_i\right) A_{i+1/2} \sin\left(\beta_{i+1/2} - \dfrac{\pi}{2}\right) \end{cases} \tag{44}$$

The force on PS and SS $F_{i+1/2}^{PS}$ and $F_{i+1/2}^{SS}$ is exerted by the pressure on PS and SS, and derived using Equation (45).

$$\begin{cases} F_{x,i+1/2}^{PS} = P_{i+1/2}^{pl} Z_{i+1/2} \left(L_{i+1}^{pl} - L_i^{pl}\right) \cos\left(\beta_{i+1/2} - \dfrac{\pi}{2}\right) \\ F_{y,i+1/2}^{PS} = P_{i+1/2}^{pl} Z_{i+1/2} \left(L_{i+1}^{pl} - L_i^{pl}\right) \sin\left(\beta_{i+1/2} - \dfrac{\pi}{2}\right) \\ F_{x,i+1/2}^{SS} = -P_{i+1/2}^{sl} Z_{i+1/2} \left(L_{i+1}^{sl} - L_i^{sl}\right) \cos\left(\beta_{i+1/2} - \dfrac{\pi}{2}\right) \\ F_{y,i+1/2}^{SS} = -P_{i+1/2}^{sl} Z_{i+1/2} \left(L_{i+1}^{sl} - L_i^{sl}\right) \sin\left(\beta_{i+1/2} - \dfrac{\pi}{2}\right) \end{cases} \tag{45}$$

Pressure gradient $(dP/dL)_n$ in the normal direction is derived through using simple radial equilibrium assumption as Equation (46). The first item in the right of Equation (46) is the pressure gradient due to the centrifugal force of the flow. The second item is the pressure gradient due to the centrifugal force of the rotating frame. The third item is the pressure gradient due to the Coriolis force.

$$\begin{aligned} \left(\frac{dP}{dL}\right)_{n,i+1/2} = & \left[\left(1-\alpha_{i+1/2}\right)\rho_{l,i+1/2} W_{l,i+1/2}^2 + \alpha_{i+1/2}\rho_{v,i+1/2} W_{v,i+1/2}^2\right] \frac{Z_{i+1/2}^2}{\varsigma_{i+1/2}^{cl}} + \rho_{m,i+1/2}\Omega^2 r_{i+1/2}^{cl} \sin\beta_{i+1/2}^{cl} Z_{i+1/2}^2 \\ & - 2\Omega\left[\left(1-\alpha_{i+1/2}\right)\rho_{l,i+1/2} W_{l,i+1/2} + \alpha_{i+1/2}\rho_{v,i+1/2} W_{v,i+1/2}\right] Z_{i+1/2}^2 \end{aligned} \tag{46}$$

where ς is the curvature radius. The pressure on PS and SS is

$$\begin{cases} P_{i+1/2}^{pl} = P_{i+1/2}^{cl} + \left(\dfrac{dP}{dL}\right)_{n,i+1/2} \dfrac{Z_{i+1/2}}{2} \\ P_{i+1/2}^{sl} = P_{i+1/2}^{cl} - \left(\dfrac{dP}{dL}\right)_{n,i+1/2} \dfrac{Z_{i+1/2}}{2} \end{cases} \tag{47}$$

According to Assumption (7), the pressure on TS and BS is the same. The force exerted on TS and BS is

$$
\begin{cases}
F_{x,i+1/2}^{TS} = -P_{i+1/2}^{cl} Z_{i+1/2} \left(L_{i+1}^{cl} - L_i^{cl} \right) \sin\vartheta \cos\beta_{i+1/2} \\
F_{y,i+1/2}^{TS} = -P_{i+1/2}^{cl} Z_{i+1/2} \left(L_{i+1}^{cl} - L_i^{cl} \right) \sin\vartheta \sin\beta_{i+1/2} \\
F_{x,i+1/2}^{BS} = P_{i+1/2}^{cl} Z_{i+1/2} \left(L_{i+1}^{cl} - L_i^{cl} \right) \sin\vartheta \cos\beta_{i+1/2} \\
F_{y,i+1/2}^{BS} = P_{i+1/2}^{cl} Z_{i+1/2} \left(L_{i+1}^{cl} - L_i^{cl} \right) \sin\vartheta \sin\beta_{i+1/2}
\end{cases} \tag{48}
$$

where ϑ is defined by $arctan[(Z_{i+1} - Z_i)/(L_{i+1} - L_i)]$, as shown in Figure 14(b). It should be noted that in this paper the force exerted on TS and BS is zero in IS because the height of channel in IS is constant and ϑ is zero. The efficiency of the impeller is defined as

$$
\eta = \frac{Po}{m\left(H_{in}^{0,is} - H_{out}^{s,mfp} \right)} \tag{49}
$$

3 Case Study

3.1 Design Case

Design requirements are listed in Table 2. The inflow is subcooled liquid. The outlet pressure is lower than the atmospheric pressure. The inlet liquid relative velocity is 10 m/s. The blade number is two, and the area factor is 1.1. The inlet radius of IS is 28 mm, and the inlet radius of MFP is 30 mm. The outlet radius of MFP’s PL is 100 mm. All thermal properties are evaluated through IAPWS in the paper.

Table 2 Design requirements and given parameters for the case

Parameters	Value
Inlet total pressure P_{in}^0	500 kPa
Inlet temperature T_{in}	110 ℃
Outlet static pressure P_{out}	15 kPa
Mass flow rate m	1000 kg/h
Rotational speed N	-3000 rpm
Inlet relative flow angle γ_{in}	45°
Outlet relative flow angle γ_{out}	70°

To present smooth and continuous distribution of the relative flow angle in MFP, second order Bezier curve fitting method is used as shown in Figure 14.

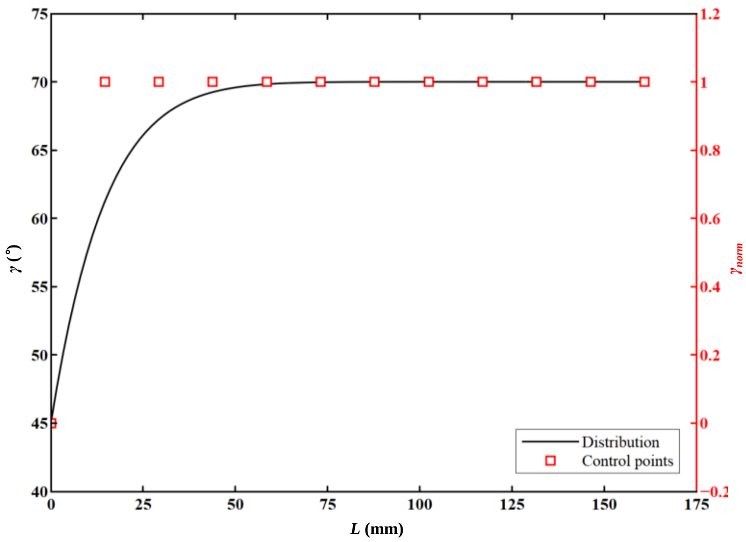

Figure 14. Relative flow angle distribution in MFP

Control points of normalized relative flow angle and normalized length are given from 0 to 1. Distribution of normalized relative flow angle γ_{norm} is derived using second order Bezier method. Distribution of relative flow angle γ is scaled from γ_{in} to γ_{out} using Equation (50) and the length is scaled between 0 and $L^{cl}_{n_{mfp}}$.

$$\gamma_i = \gamma_{in} + \gamma_{norm,\,i}\left(\gamma_{out} - \gamma_{in}\right) \tag{50}$$

The distribution of pressure along MFP's CL is given through the control points of normalized pressure using the same method of the relative flow angle. The given pressure is shown in Figure 15. The vaporization does not happen immediately when the local pressure is lower than the saturation pressure at the inlet temperature, which is called the pressure undershoot. Long enough channel with low pressure should be provided to boost the vaporization. Thus, the pressure should decrease significantly from the inlet to the middle of the channel and gradually from the middle to the outlet of the channel.

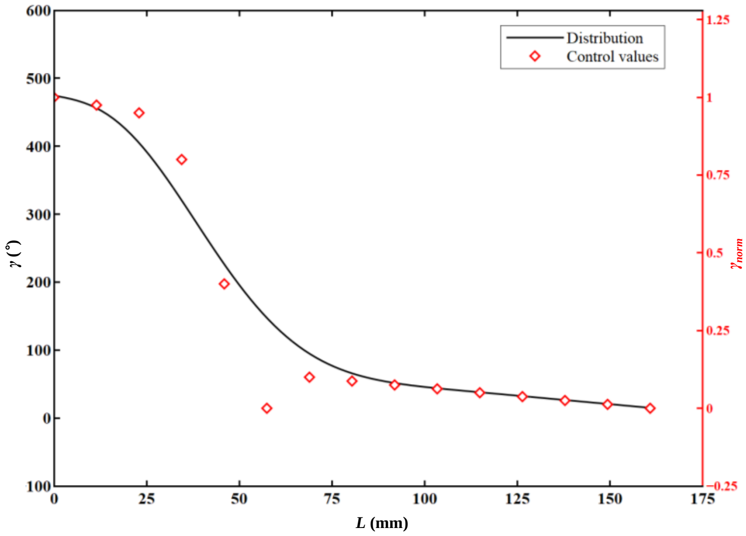

Figure 15. The given pressure distribution in MFP

After using the program of designing CL, positions of CL can be determined as shown in Figure 16(a). Because for MFP's CL, the inlet radius is 30 mm and γ_{in} is 45° as shown in Figure 14, the initial position (x_1, y_1) is (0.03, 0), θ_{in} is 0°, γ_{in} is 45° and β_{in} is 45° as shown in Figure 16(b).

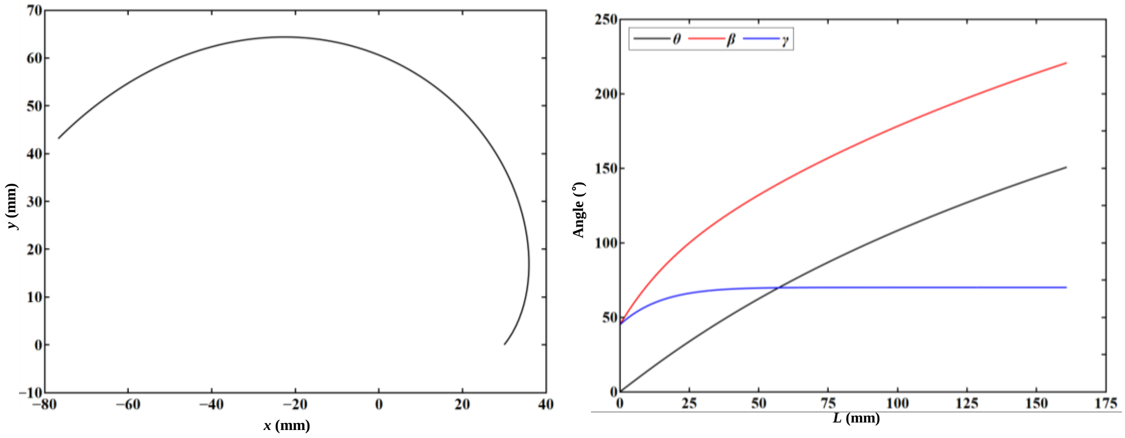

(a) CL (b) Polar angle, blade angle and relative flow angle

Figure 16. The designed CL profile and polar and blade angles

After using the program of designing area and IS, all parameters can be derived. The width of the channel and void fraction is shown in Figure 17 (a). The saturation pressure at the inlet temperature, P_{in}^{sat}, is 143 kPa. At $R^{cl} = 53.9\,mm$, the local pressure P reaches P_{in}^{sat}, the liquid temperature is equal to the local saturation temperature, and the vapour starts vaporizing. At $R^{cl} = 56.5\,mm$, Z reaches the minimum 2.4 mm and the void fraction α is 0.0048, and this position is called the throat. After the throat, liquid vaporizes remarkably, and the width of the channel increases significantly. In IS, the pressure decreases sharply due to the significant reduction of the width, as shown in Figure 17(b).

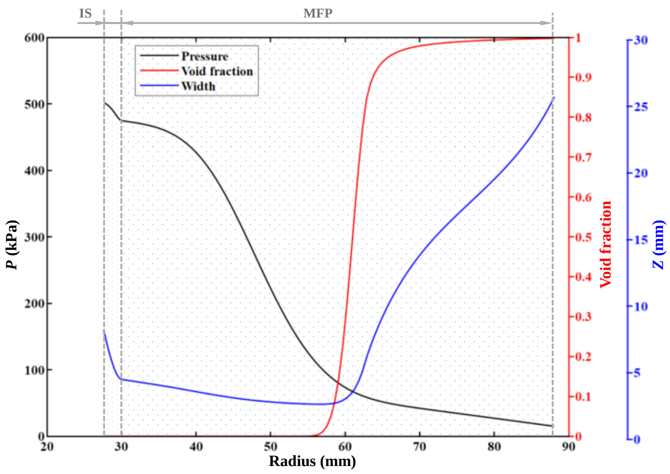

(a) Pressure, void fraction and width

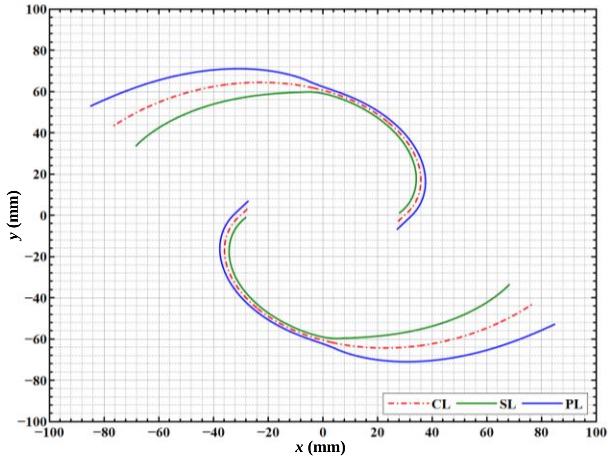

(b) Shape of MFP

Figure 17. Results of the design

After using the program of evaluation of output power, the output power is 480 W, the torque is 1.53 N·m, and the efficiency of the impeller is 9.27 %.

3.2 Numerical Simulation

In this paper, CFX is used to validate the design method through comparing CFD results and one-dimensional design results in the designed case. Using Euler multiphase flow model and the thermal phase change model, CFX can predict the flow field of flashing. Wolfert model[58] is used to calculate Nusselt number between the liquid and the vapor. The SST turbulence model is launched to model the turbulent flow in the channels and the bubble number density is set as 5×10^{7}. Rane et al.[31–34] have introduced the mathematical models and model parameters of CFX for simulating ROTPT.

3.2.1 Validation of CFX

The RMIT's ROTPT published by Date et al.[29] is simulated in CFX to check the validity of CFD on ROTPT. Geometry model of the ROTPT is built and structural mesh is generated in ICEM as shown in Figure 18. A thin inlet tube hub is set in the core of the inlet tube to set the periodic boundary to reduce the total number of elements. The number of elements is 258,640. The total pressure and temperature are given at the inlet boundary and the static pressure is set at the outlet boundary.

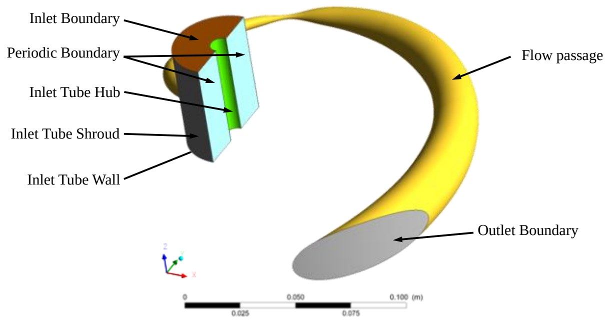

(a) Geometry

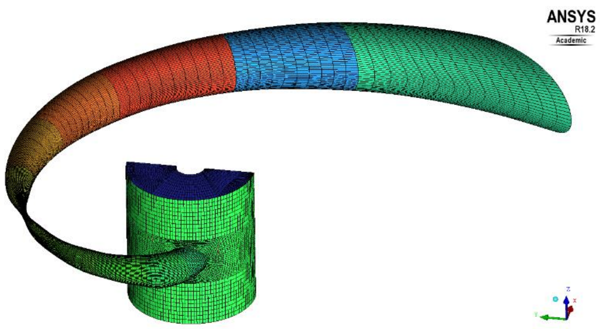

(b) Mesh

Figure 18 Geometry and mesh of RMIT's ROTPT

According to Date et al.[29], at the maximum output power point, the inlet pressure is 400 kPa, the inlet temperature is 117.1℃, the outlet pressure is 7.7 kPa, the mass flow rate is 822 kg/h, the rotational speed is 4614 rpm, the output power is 1.33 kW, and the efficiency is 17%. CFD results show that the CFD mass flow rate is 766 kg/h and the CFD output power is 1.12 kW.

3.2.2 CFD model of the design case

Using the design results, the geometry model of the computational domain is built, as shown in Figure 19(a). Because the number of blades is two in this paper, the computational domain is half of the geometry. Two periodic boundaries are set in the domain of the inlet tube. For the convenience of generating the mesh, an inlet tube hub is set in the core of the inlet tube. The structural mesh is generated in ICEM, as shown in Figure 19(b).

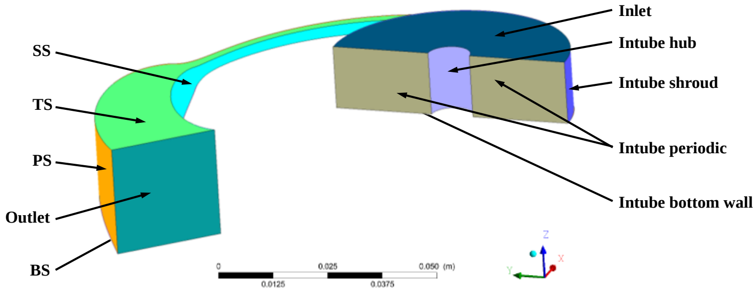

(a) Geometry

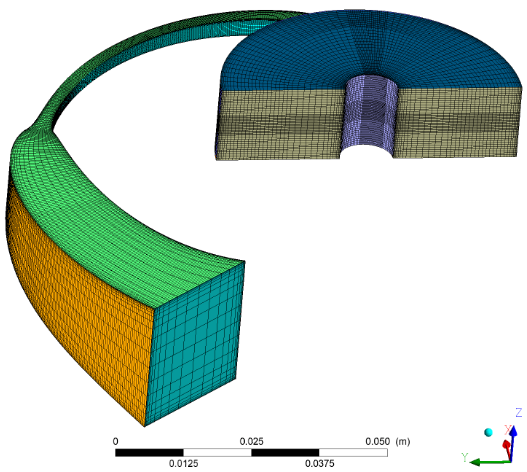

(b) Mesh

Figure 19. Computational domain of the design case

By using the same mathematical models as the validation case, comparison of the performance between the design and CFD is shown in Table 3. Design values of mass flow rate, output power agree and efficiency with those of CFD.

Table 3 Performance of design and CFD

Parameters	Design	CFD
Inlet total pressure P_{in}^{0}	500 kPa	500 kPa
Inlet temperature T_{in}	110 ℃	110 ℃
Outlet static pressure P_{out}	15 kPa	15 kPa
Outlet liquid temperature $T_{l,out}$	89 ℃	84 ℃
Mass flow rate m	1000 kg/h	997 kg/h
Output power of the impeller Po	480 W	454 W
Output power at IS Po_{is}	117 W	116 W
Output power at MFP Po_{mfp}	875 W	845 W
Output power at the outlet Po_{out}	510 W	507 W
Efficiency η	9.27%	8.81%

4 Flow Details and Discussion

4.1 Average flow parameters in the channel

Averaged flow parameters are calculated in cross-sections which are perpendicular to the flow direction, as shown in Figure 2(b). Distribution of pressure is shown in Figure 20(a) and the deviation between the design and CFD is illustrated in Figure 20(b). Distribution of the design has a similar tendency as CFD, but there is a certain deviation between them.

In respect of the pressure, pressure of CFD is higher than pressure of design in the MFP upstream the throat and lower than pressure of design at the downstream channel after the throat, as shown in Figure 20(a). The deviation upstream the throat is caused by the incidence near the inlet of the channel. The deviation after the throat is determined by the pressure undershoot near the throat. In Region A, pressure of CFD has a larger gradient than pressure of design. Region A is in the channel of MFP at the downstream channel after the throat.

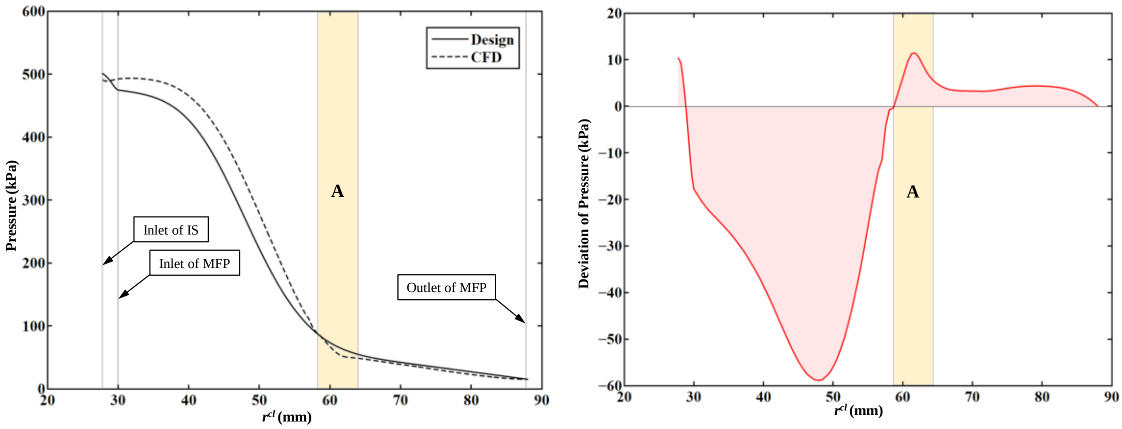

(a) Pressure (b) Deviation

Figure 20 Distribution of pressure and deviation between design and CFD

In respect of the void fraction, design agrees with CFD in the whole channel since the maximum deviation is less than 0.05, as shown in Figure 21. It indicates that the design method can predict the inception and the development of the flashing with high accuracy. The tiny disagreement is caused by the difference of the interphase mass flow rate between design and CFD as shown in Figure 23(a), and mainly appears in the inception of the flashing at Region B which is at the downstream channel after the throat. The maximum deviation appears at r^{cl}=60.7 mm which is at the upstream channel before the maximum deviation of the interphase mass flow rate.

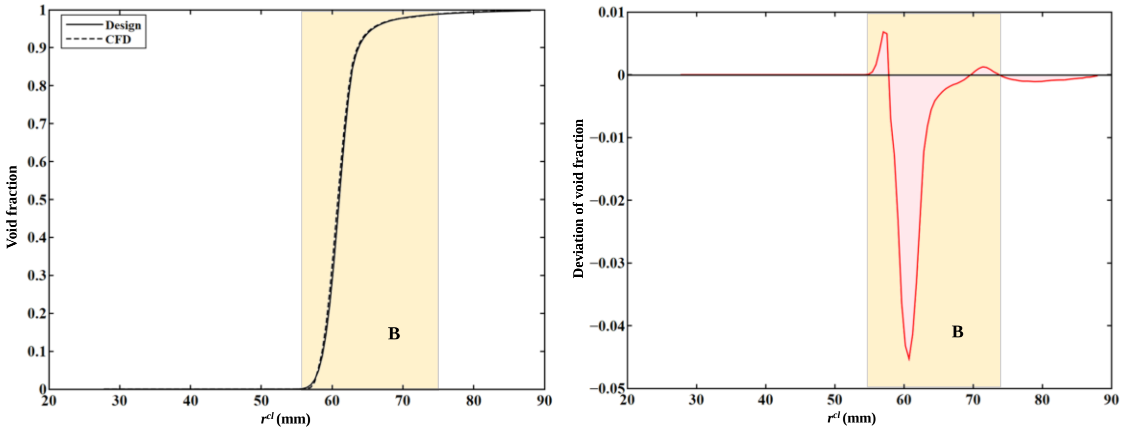

(a) Void fraction (b) Deviation

Figure 21 Distribution of void fraction and deviation between design and CFD

The distribution of the velocity is shown in Figure 21(a). The velocity of the design increases smoothly, but the velocity of CFD fluctuates near region A. The vapour velocity is not zero before the throat because the minimum void fraction is set to be 1.0^{-6}. The distribution of the slip ratio is shown in Figure 22(b). The slip ratio of the absolute velocity is larger than that of relative velocity in CFD and design except for the inlet region. Both the maximum slip ratio of the absolute velocity and the relative velocity locates near the throat for CFD and design. There is certain deviation between CFD and design. For CFD, the slip ratio fluctuates in Region C, and the global maximum slip ratio of relative velocity is 1.23 at r^{cl}=61.3 mm. At the downstream channel after Region C, the slip ratio remains in increasing smoothly and decreasing after the local peak value. But for design, the slip ratio curve is much smoother, and the global maximum slip ratio of relative velocity is 1.15 at r^{cl}=61.3 mm. After the global maximum slip ratio position, the slip ratio keeps decreasing until the outlet of the channel.

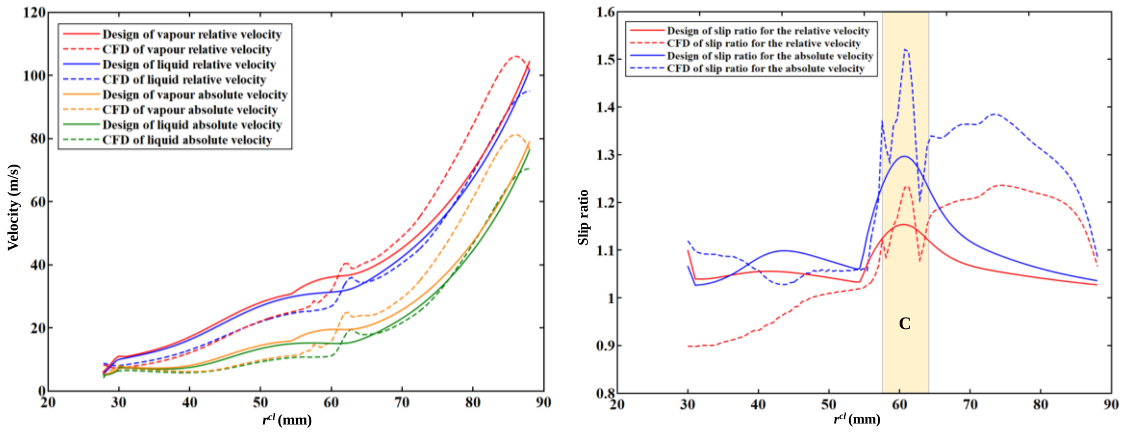

(a) Liquid and vapour velocity (b) Slip ratio

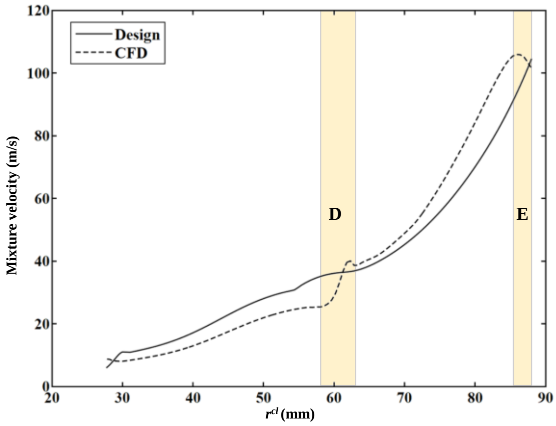

(c) Mixture velocity

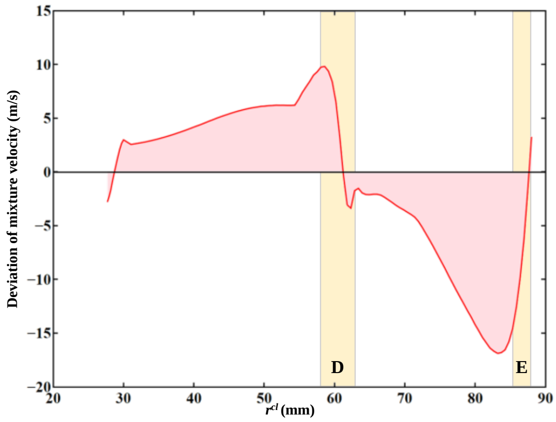

(d) Deviation of mixture velocity

Figure 22 Distribution of velocity, slip ratio, mixture velocity and deviation of mixture velocity along the channel

The mixture velocity W_m is defined as $\alpha W_v + (1 - \alpha) W_l$. The distribution of mixture velocity is shown in Figure 22(c). In the one-dimensional design, the mixture velocity increases with the length of the channel. CFD results show that there is fluctuation in Region D and reduction of the mixture velocity in Region E. The deviation between design and CFD is shown in Figure 22(d). The maximum deviation of the mixture velocity is 16.9 m/s at r^{cl}=81.6 mm in Region E near the outlet of the channel.

Liquid temperature and vapour temperature is shown in Figure 23. Because the vapour temperature is set to be the saturation temperature at local pressure, the vapour temperature has similar trends as the pressure. In the downstream channel after the throat, the liquid temperature of CFD is lower than the design.

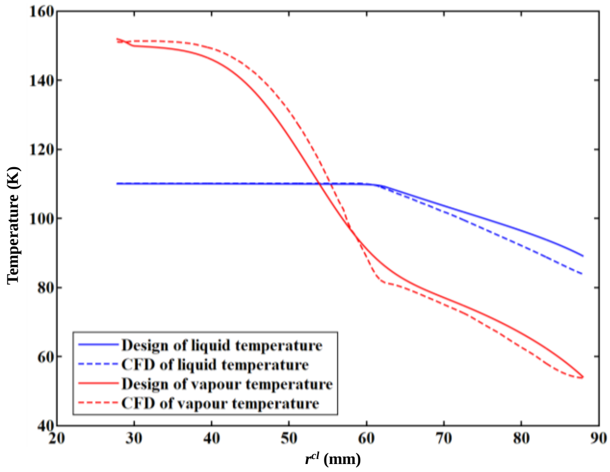

Figure 23 Distribution of vapour and liquid temperature

The interphase mass flow rate is the mass flow rate transferred from the liquid to the vapour per volume, as shown in Figure 24(a). Design distribution and CFD have the similar trend, but the maximum interphase mass flow rate of CFD is lower than that of design, and the position for the maximum value in CFD is at the upstream location of the position in design. The heat transfer coefficient and Nusselt number are shown in Figure 24(b). For the heat transfer coefficient, CFD shows the similar trend as design except the inlet region. At r^{cl}=54.3 mm, heat transfer coefficient of design reaches the local peak value while CFD results show that the peak value locates at r^{cl}=56.0 mm. For Nusselt number, CFD results show the similar trend as design in almost the whole channel except the outlet region of the channel.

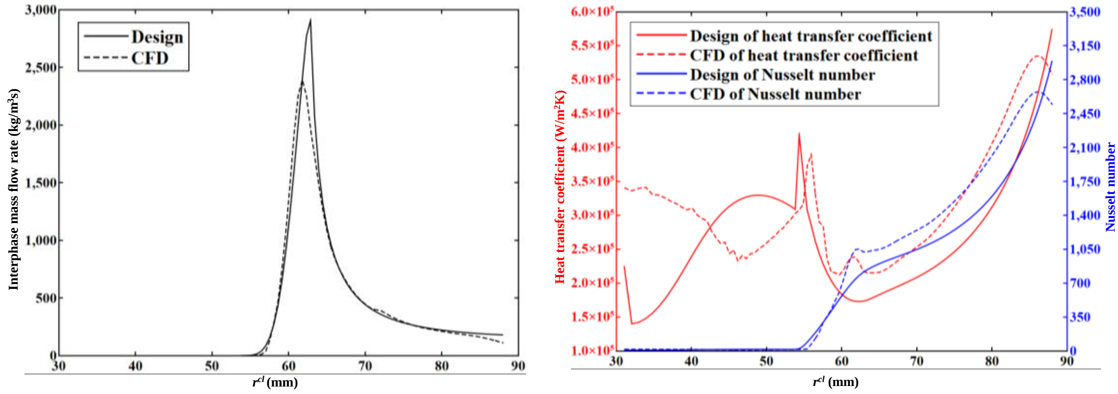

(a) Interphase mass flow rate (b) Heat transfer coefficient and Nusselt number
Figure 24 Distribution of interphase mass flow rate, heat transfer coefficient and Nusselt number

4.2 Three-Dimensional Flow

The aforementioned regions are concluded in Figure 25. All regions except Region E are located mainly near the throat. Region E is near the outlet of the channel. It suggests that the effects of the three-dimensional flow on the averaged parameters are evident in these regions.

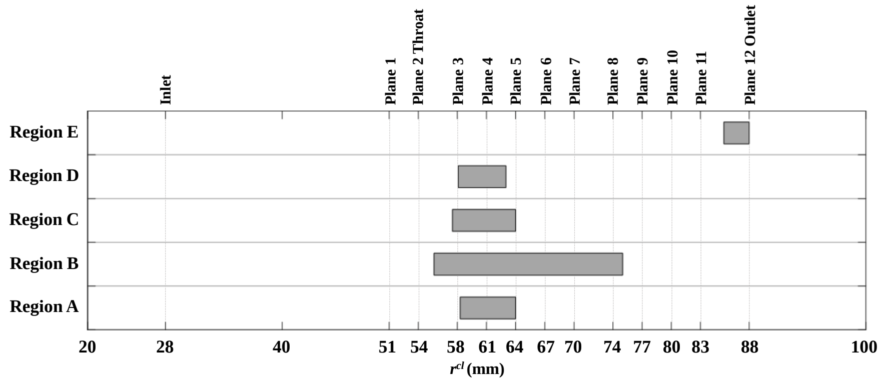

Figure 25 Location of different regions

For analyzing the three-dimensional flow in these regions, twelve cross-sectional planes are cut along the channel, as shown in Figure 25 and Figure 26. These planes are perpendicular to the flow direction of the channel and covers all the aforementioned regions. Plane 2 locates at the throat of the channel. Detailed geometrical parameters of these planes are listed in Table 4.

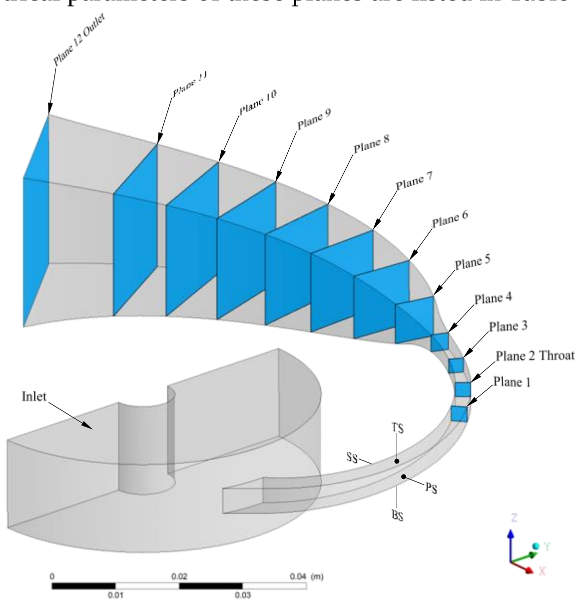

Figure 26 Cross-sectional planes specified in the channel

Table 4 Center points of the planes

Planes	x (mm)	y (mm)	z (mm)	Z (mm)	β (°)
Plane 1	23.8	45.3	0.0	2.5	131.8
Plane 2	16.7	51.7	0.0	2.4	142.0
Plane 3	8.5	56.9	0.0	2.4	151.4
Plane 4	-0.3	60.7	0.0	3.1	160.3
Plane 5	-9.7	63.2	0.0	7.5	168.7
Plane 6	-19.3	64.3	0.0	11.2	176.7
Plane 7	-28.9	64.1	0.0	13.8	184.3
Plane 8	-38.4	62.7	0.0	15.8	191.5
Plane 9	-47.7	60.1	0.0	17.6	198.5
Plane 10	-56.7	56.4	0.0	19.3	205.1
Plane 11	-65.1	51.8	0.0	21.3	211.5
Plane 12	-76.7	43.1	0.0	25.5	220.7

The pressure on surfaces of the channel is shown in Figure 26. For design, the pressure is assumed to be constant along the span direction, and the pressure in linearized along the normal direction based on the simple radial equilibrium hypothesis. For CFD, the pressure is ununiform along the span direction near the inlet of the channel as shown in Figure 27(a) and in the divergent part of the channel especially on Plane 4, 5, 6, 7, 8, 10 and 11. The pressure on PS is always higher than the pressure on SS on Plane 4 and 5. Plane 4 and Plane 5 are located in Region A as shown in Figure 25. In these planes, a high-pressure region appears inside the channel. Along the flow direction, the high-pressure region stems from PS, appears in the channel within Region A, and returns back to PS. The development of the high-pressure region is of high relevance with the deviation between design and CFD in Region A, which is shown in Figure 20. The pressure on Plane 12 is uniform because the computational domain ends at Plane 12.

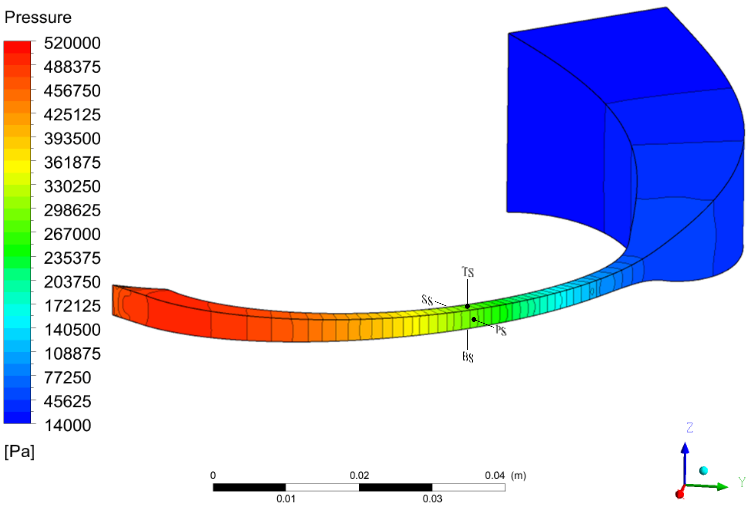

(a) Surfaces of the channel

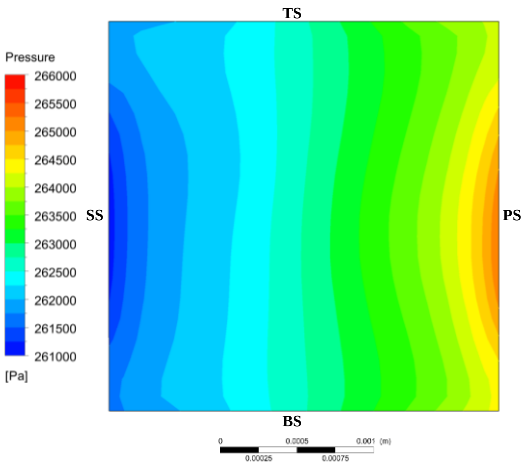

(b) Plane 1

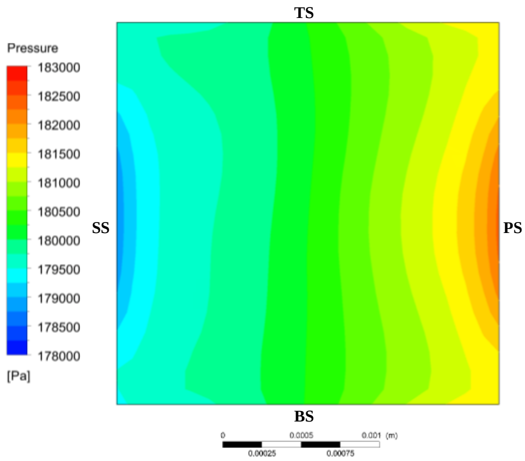

(c) Plane 2

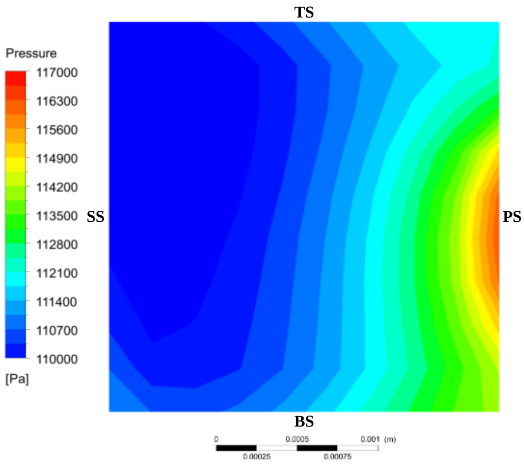

(d) Plane 3

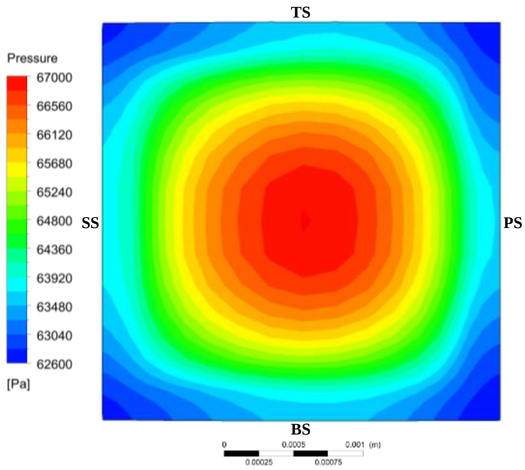

(e) Plane 4

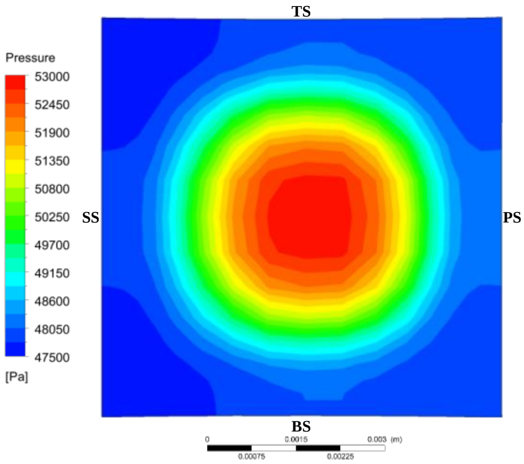

(f) Plane 5

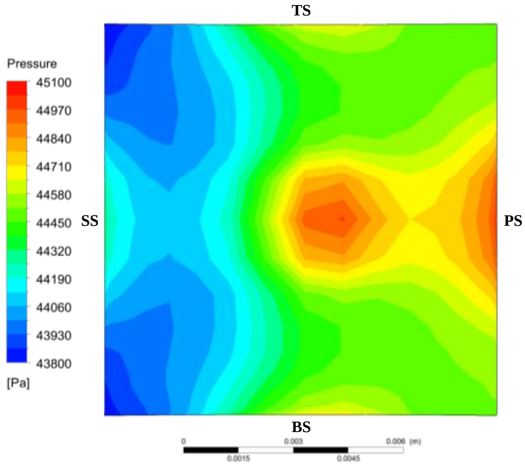

(g) Plane 6

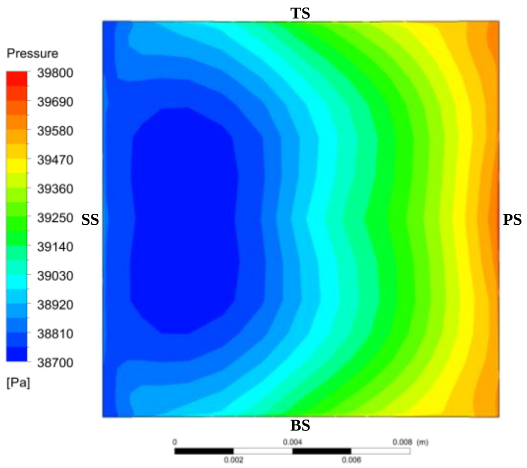

(h) Plane 7

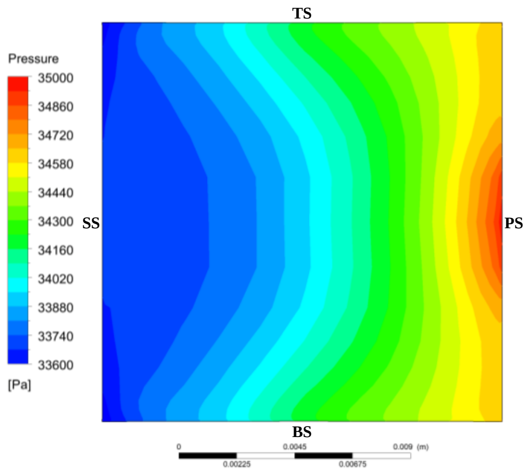

(i) Plane 8

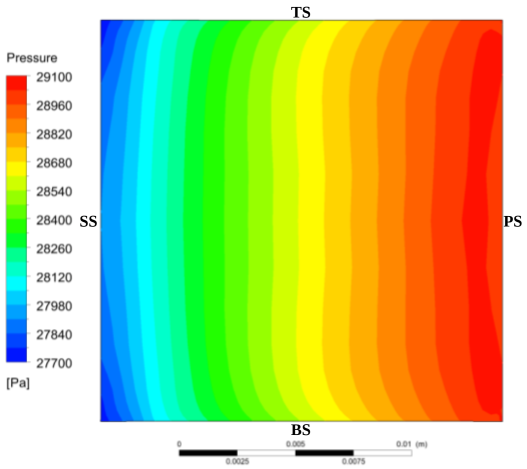

(j) Plane 9

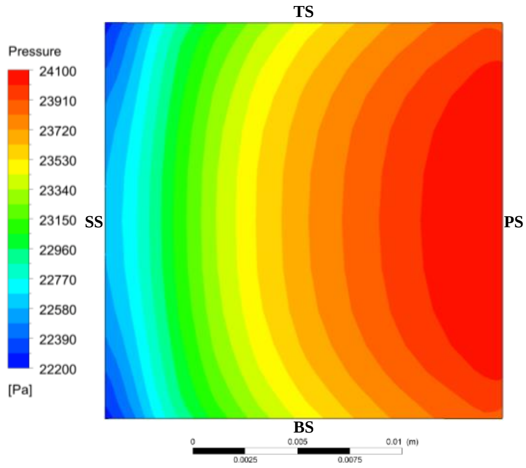

(k) Plane 10

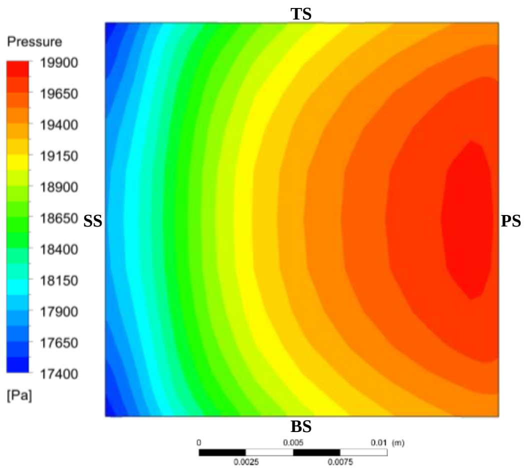

(l) Plane 11

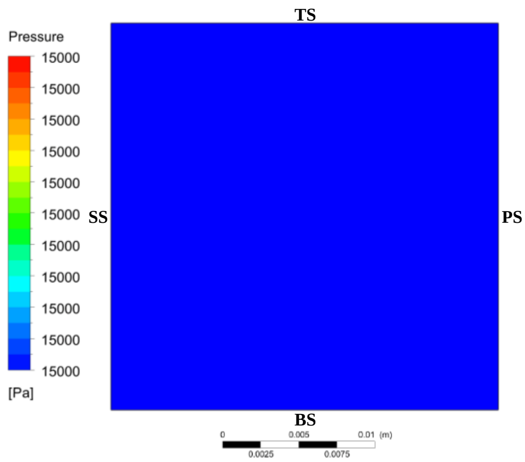

(m) Plane 12

Figure 27 Contour lines of pressure on walls and cross planes of the channel

The process of vapour generation, growth and development is shown in Figure 28. For the design, the void fraction is constant on the normal direction and span direction. For the CFD, it is obvious that the generation of the vapour is heterogeneous and there are low void fraction areas on the walls where liquid reattaches. The generation of vaporization starts from walls and develops into the channel. On

Plane 3, the vapour is generated on most of SS, sections of TS and BS near SS, and corners of PS near TS and BS shown in Figure 28(b). On Plane 4, it is shown that the vapour has already covered all the walls, while there is liquid and vapour mixture in the middle area of the plane. On Plane 5 and 6, the vapour keeps growing. On Plane 6 and Plane 7, there is liquid attached on the walls.

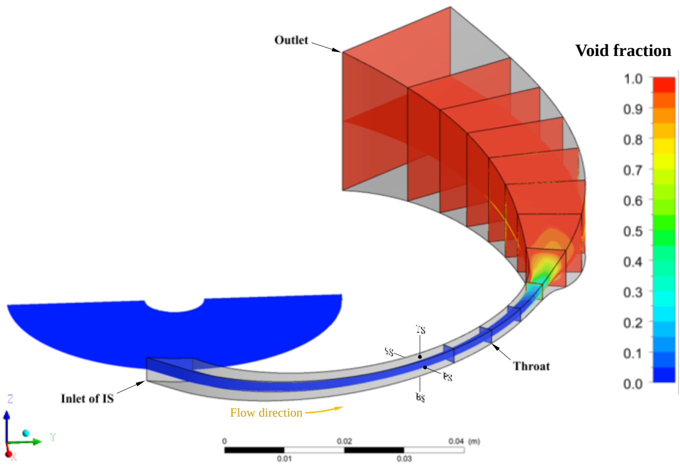

(a) Planes in the channel

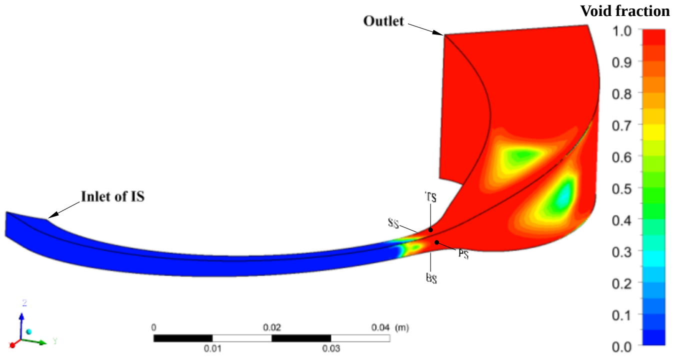

(b) Surfaces of the channel

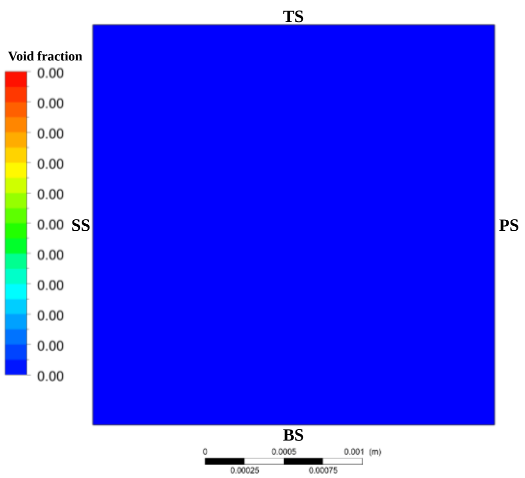

(c) Plane 1

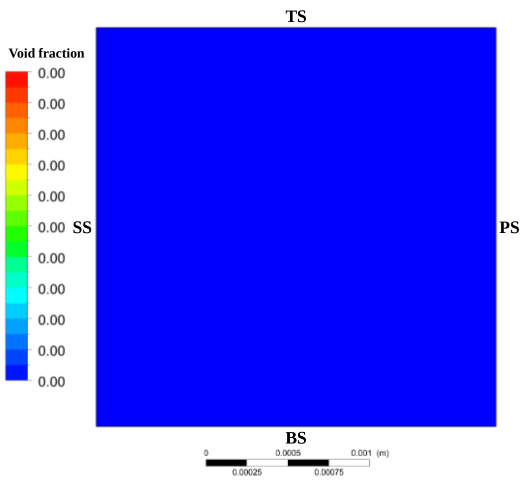

(d) Plane 2

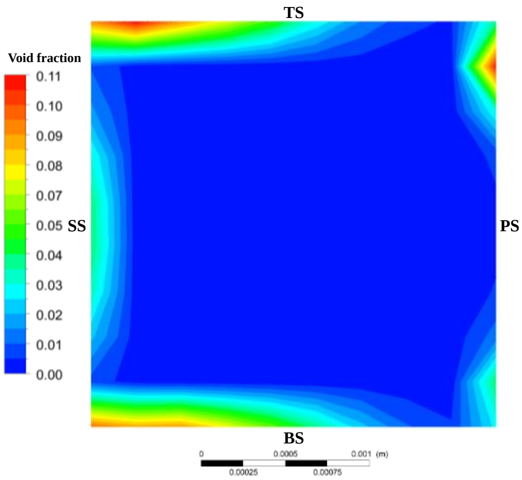

(e) Plane 3

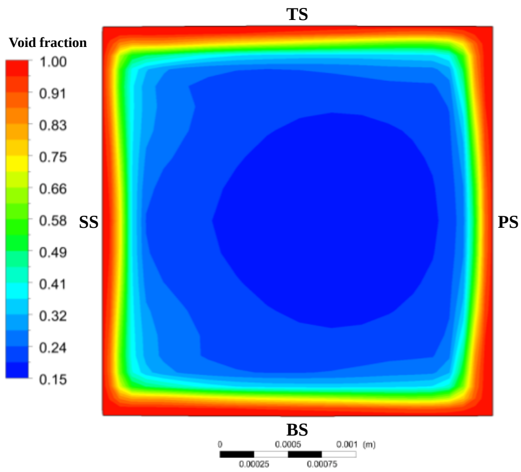

(f) Plane 4

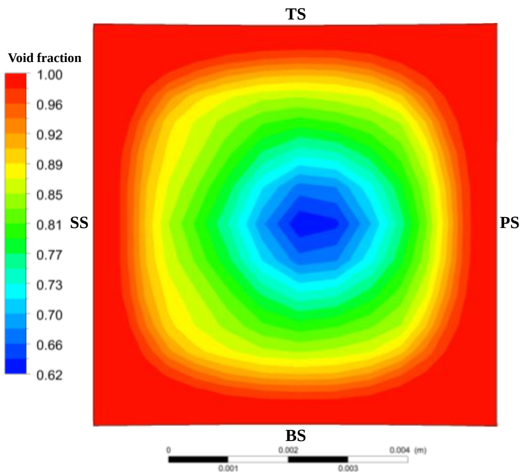

(g) Plane 5

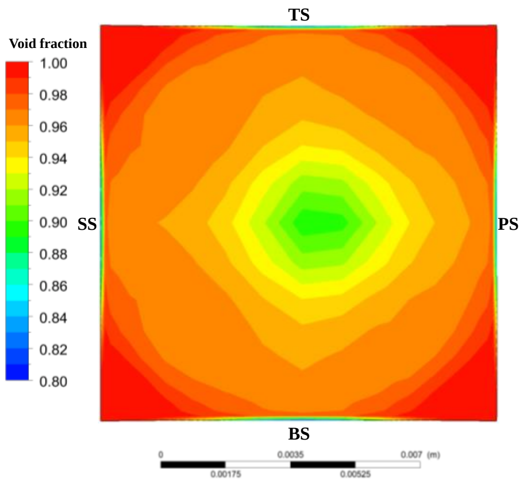

(h) Plane 6

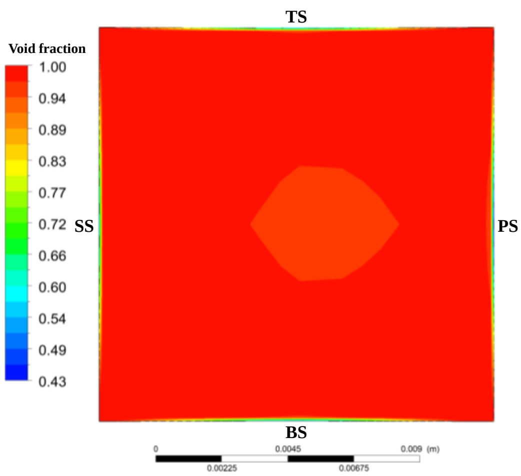

(i) Plane 7

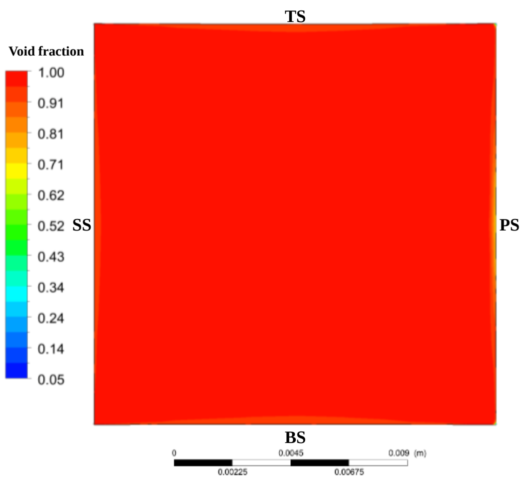

(j) Plane 8

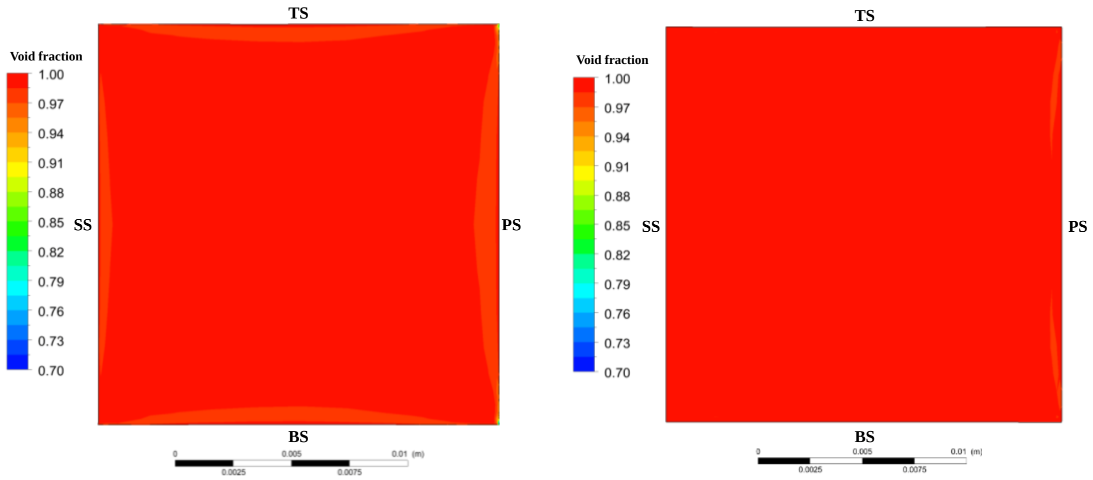

(k) Plane 9 (l) Plane 10

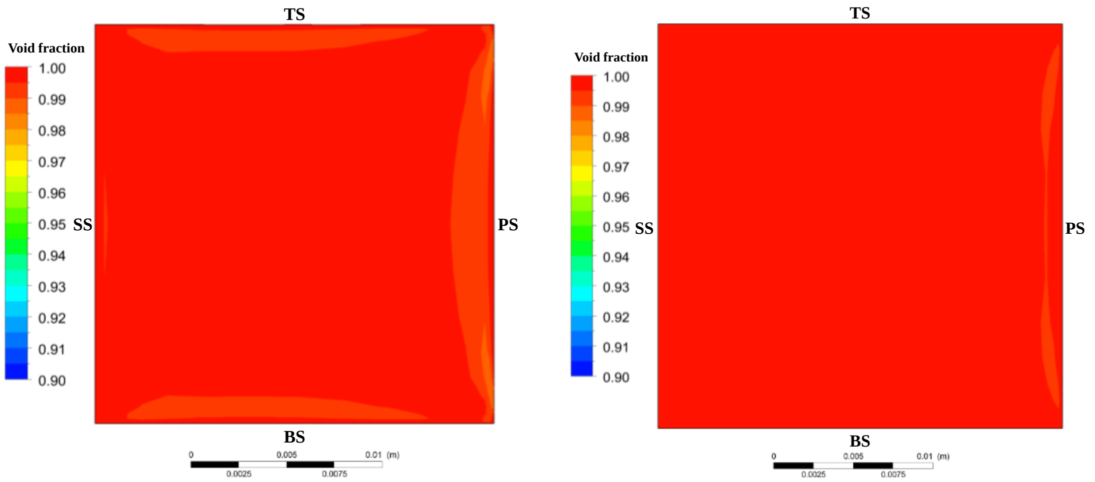

(m) Plane 11 (n) Plane 12

Figure 28 Contours of void fraction in the channel

The liquid relative velocity is shown in Figure 29. For the design, the relative velocity is homogenous on the planes based on the assumption. For the CFD, it is obvious that there are high velocity regions near SS. On Plane 1, 2 and 3, the profile of the velocity is similar although the magnitude is different. From Plane 5 to Plane 12, there are high velocity regions in the four corners. From Plane 6 to Plane 9, there are low speed regions near the walls.

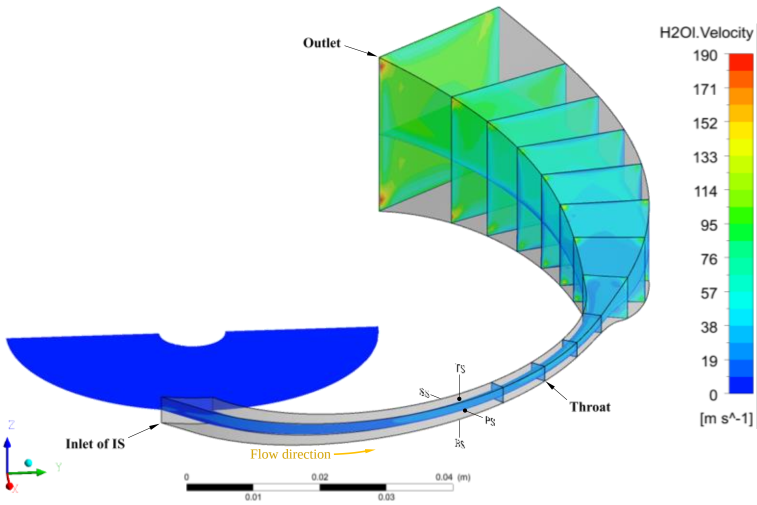

(a) Planes in the channel

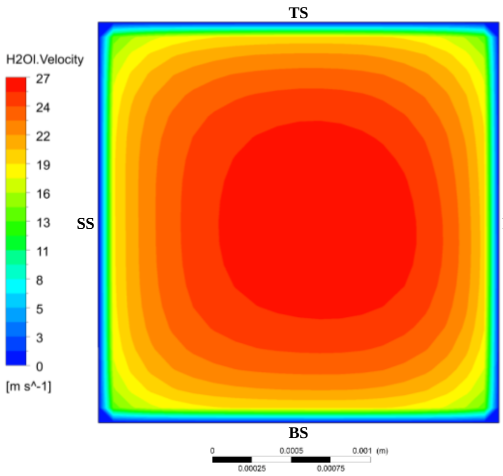

(b) Plane 1

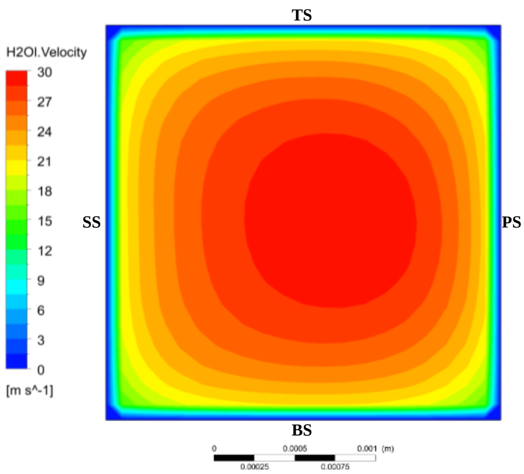

(c) Plane 2

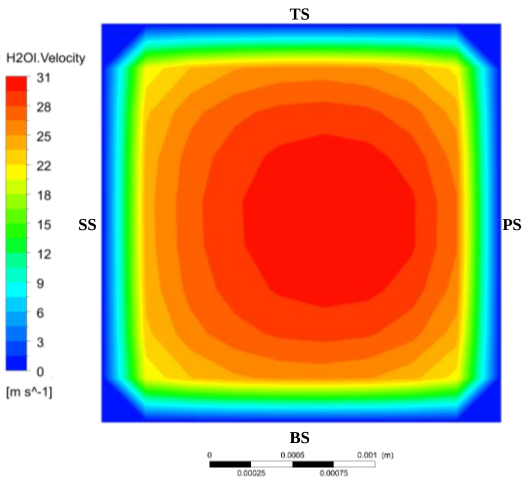

(d) Plane 3

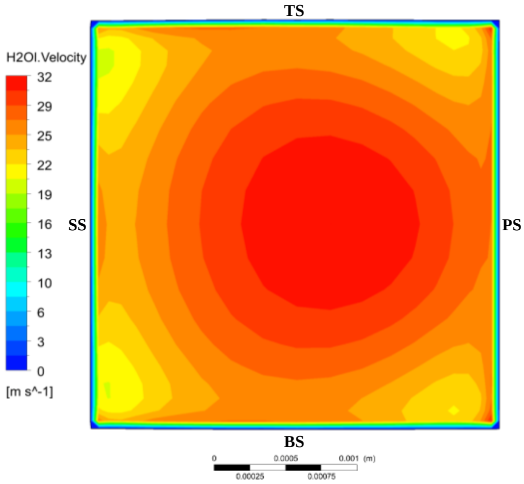

(e) Plane 4

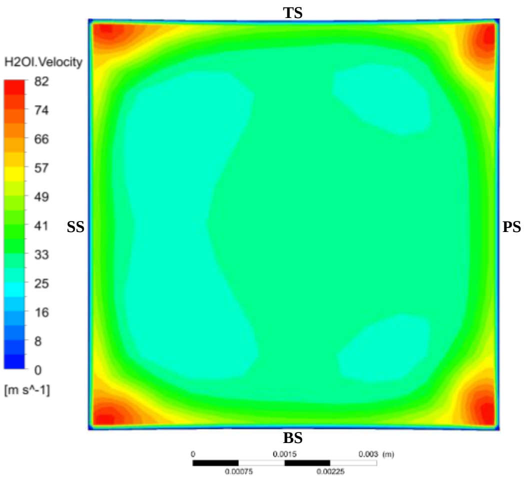

(f) Plane 5

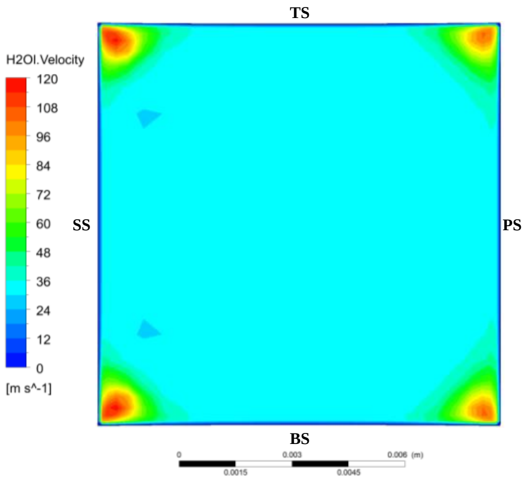

(g) Plane 6

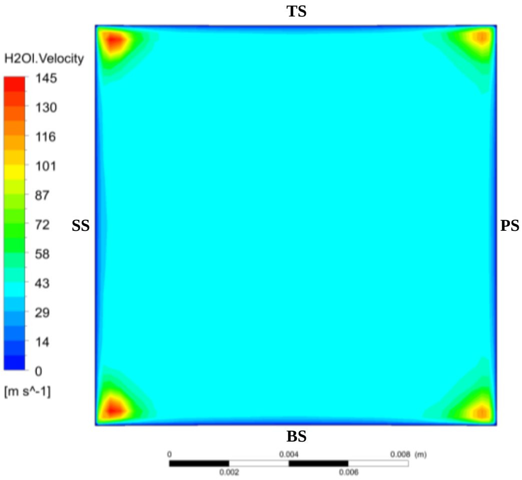

(h) Plane 7

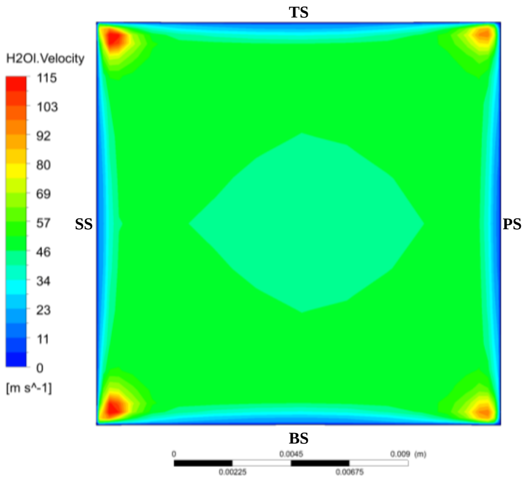

(i) Plane 8

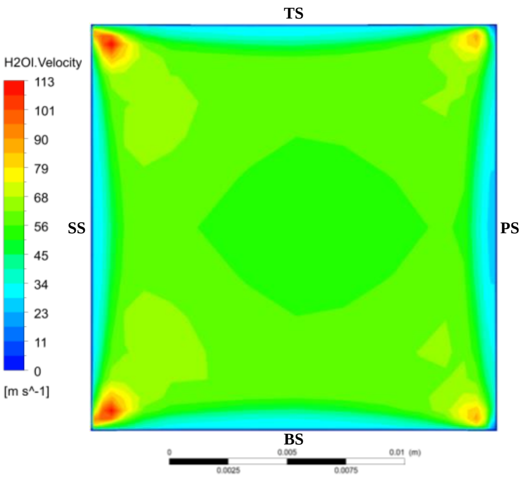

(j) Plane 9

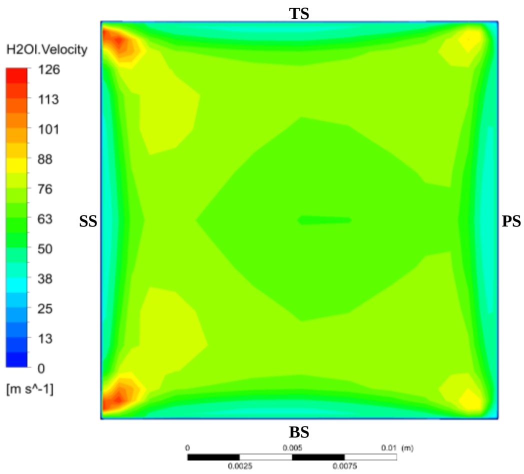

(k) Plane 10

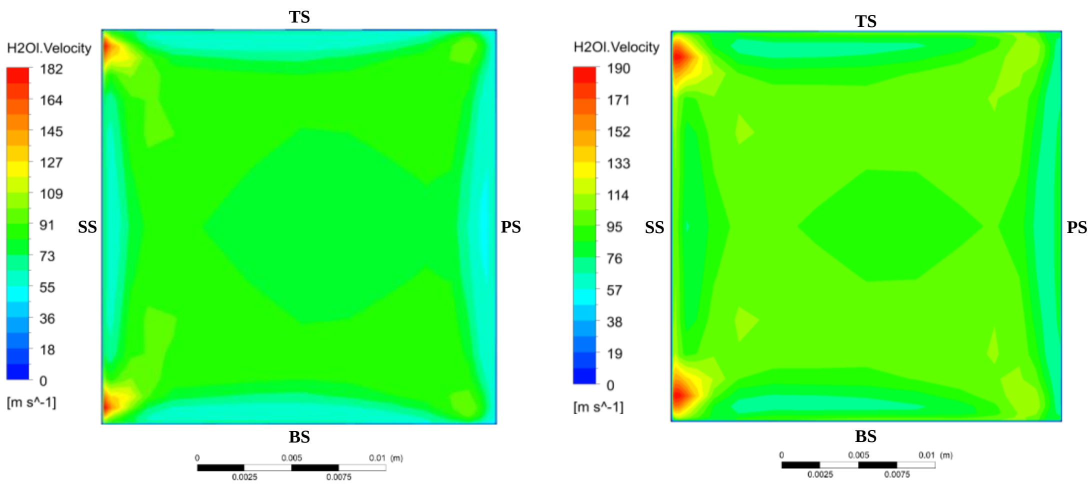

(l) Plane 11 (m) Plane 12

Figure 29 Contours of liquid relative velocity in the channel

5 Conclusions

In this paper, an inverse mean-line design method of ROTPTs is presented. It considers various non-equilibrium effects such as slip between phases, nonequilibrium properties, and interphase heat transfer. Under the implementation of the distribution of the pressure and the blade angle, the flow path centerline, channel area and flow parameter distribution along the flow direction can be calculated. According to the simple radial equilibrium principle, the design method can also evaluate the pressure distribution on the pressure surface and the suction surface and deduce impeller performance parameters.

Using the proposed design method, a ROTPT has been designed for the condition where the total inlet pressure is 500 kPa, the inlet temperature is 110°C, the outlet static pressure is 15 kPa, and the mass flow rate is 1000 kg/h. According to the design, the output power is 480 W, the torque is 1.53 N·m, and the efficiency is 9.23%. Through the numerical simulation, which is validated using experimental results, it shows that the output power is 454 W, the mass flow rate is 997 kg/h, the efficiency is 8.81%.

Through analysis on the average flow parameters along the flow direction in CFD results, the distribution of void fraction agrees well with the design, while there is a certain deviation in the pressure. Through analysis on contours of pressure, void fraction and liquid relative velocity along the channel, significant three-dimensional flow effects are found in the channel. The generation of the vapour starts from the walls of the channel and develops into the middle of the channel. There is also reattachment of the liquid in the divergent part of the channel. There is a high-pressure region in the middle of the channel near the throat and high relative velocity region near the four corners of the channel. In future research, the three-dimensional effects, such as the incidence near the inlet and pressure undershoot, on the turbine performance will be evaluated in the one-dimensional design. Design parameters, including the area ratio and the maximum radius, will be optimized.

Acknowledgement

This research is supported by EPSRC (EP/P028829/1, EP/N020472/1, EP/R003122/1) in United

Kingdom. Authors would like to thank Dr Wenguan Li for reviewing this paper. Authors would also like to thank Dr Abhijit Date, RMIT, Australia, for providing the reference turbine test data for development and validation of the CFD model.

Nomenclature

A	Area
A_{int}	Interfacial area between liquid and vapour
C	Absolute velocity
C_D	Drag coefficient
Cp	Specific heat capacity at constant pressure
D_b	Bubble diameter
f	Friction coefficient
h	Height of the channel
h_{lv}	Heat transfer coefficient between liquid and vapour
H	Enthalpy
Ja	Jakob number
L	Length
La	Laplace number
m	Mass flow rate
m_{lv}	Mass flow rate transferred from liquid to vapour per volume
n	Node
N	Rotational speed
N_b	Bubble number density
Nu	Nusselt number
P	Pressure
Pe	Peclet number
Po	Output power
Q	Arbitrary point
r	Radius
R	Set value of the radius from the design requirement
Re	Reynold number
s	Direction
S	Slip ratio
T	Temperature
T_{sup}	Superheat of the liquid
To	Torque
x, y, z	Cartesian coordinate axes
x_v	Mass fraction
Y	Two phase friction factor
Z	Width of the channel

Greek Symbols

α	Void fraction
β	Blade angle

γ	Relative flow angle
η	Efficiency
θ	Polar angle for a point on the Cartesian coordinate
υ	Kinetic viscosity
Π	Coordinate system
Π^c	Coordinate system based on a movable point along CL
Π^s	Coordinate system based on the rotating center of the impeller
ρ	Density
σ	Surface tension
τ_l	Length ratio
τ_z	Width factor
ϕ	Arbitrary parameter
Φ	Two-phase frictional pressure reduction factor
χ	Thermal diffusivity
Ω	Angular velocity

570 Superscripts

0	Total quantity
n	Normal direction
o	Coordinate system based on the rotating center
t	Relative flow direction

571 Subscripts

ce	Centrifugation
f	Friction
l	Liquid
i	Arbitrary node
in	Inlet
m	Mixture
out	Outlet
s	Isentropic quantity
v	Vapour

572 Abbreviations

CFD	Computational fluid dynamics
CL	Centerline
BS	Bottom side
FVM	Finite volume method
IHE	Isentropic homogenous equilibrium
IS	Inlet section
IT	Inlet tube
MFP	Main flow passage
OL	Outlet line
PL	Pressure line
PS	Pressure side

ROTPT	Radial outflow two-phase turbine
RITPT	Radial inflow two-phase turbine
SL	Suction line
SS	Suction side
TPIT	Two-phase impulse turbine
TPRT	Two-phase reactional turbine
TPT	Two-phase turbine
TS	Top side

Appendix A: Procedure of the whole design method

As shown in Figure 8, the procedure of the whole design method is

1. Assume the static pressure P_1^0 at the inlet of MFP, the width Z_n^0 at the outlet of MFP and the length ratio τ_l^0.
2. Design CL of MFP using the given distribution of blade angle.
3. Design the area of MFP using the given distribution of pressure and derive all geometry and flow parameters MFP.
4. Check the error of the outlet width and the error of the length ratio. Iterate step 2 and step 3 until required tolerance is reached.
5. Design IS, check the inlet pressure error and iterate the whole design process using updated values.
6. Evaluate the output power of the impeller.

Appendix B: Procedure of the design of MFP's CL

As shown in Figure 9, the procedure for the program of the design of MFP's CL is

1. Prepare flow and geometrical parameters at node i.
2. Assume the blade angle $\beta_{i+1}^{cl,0}$ at node $i+1$.
3. Derive geometrical parameters of node $i+1$ using Equation (B.1).

$$\begin{cases} x_{i+1}^{cl} = x_i^{cl} + \Delta L \cos \beta_{i+1/2}^{0,cl} \\ y_{i+1}^{cl} = y_i^{cl} + \Delta L \sin \beta_{i+1/2}^{0,cl} \\ \theta_{i+1}^{cl} = \arctan\left(y_{i+1}^{cl} / x_{i+1}^{cl} \right) \end{cases} \tag{B.1}$$

4. Derive the corrected blade angle $\beta_{i+1}^{cl,*}$ at node $i+1$ using the given distribution of flow angle and Equation (B.2).

$$\beta_{i+1}^{cl,*} = \theta_{i+1}^{cl} - \gamma_{i+1}^{cl} \tag{B.2}$$

5. Check the error of the relative flow angle and iterate until required tolerance is reached.
6. Loop node number i from 1 to $n_{mfp} - 1$.

Appendix C: Procedure of the design of MFP's area

As shown in Figure 10, the procedure for the program of the design of MFP's area is

1. Prepare all parameter values at node i.
2. Assume the liquid temperature $T_{l,i+1}^0$ at node $i+1$, and derive thermal properties at node $i+1$ and $i+1/2$.

3. Assume the slip ratio S_{i+1}^0, the area A_{i+1}^0 and the vapour volume fraction α_{i+1}^0 at node $i+1$.
4. Derive the interphase mass flow rate $m_{i+1/2}^i$, liquid mass flow rate $m_{l,i+1}$ and vapour mass flow rate $m_{v,i+1}$ at node $i+1$ using Equations (10-17) and (C.1).

$$\begin{cases} m_{l,i+1} = m/B_N - \sum_{k=1}^{i} m_{k+1/2}^i \\ m_{v,i+1} = \sum_{k=1}^{i} m_{k+1/2}^i \end{cases} \tag{C.1}$$

5. Derive the slip ratio S_{i+1} and the corrected vapour volume fraction α_{i+1}^* using Equations (19) and (20) at node $i+1$.
6. Check the vapour volume fraction error and use the corrected value to iterate until the required tolerance is reached.
7. Derive $(dP/dL)_{f,i+1/2}$ using Equations (20-29), $W_{l,i+1}$ and $W_{v,i+1}$ using Equation (C.2).

$$\begin{cases} W_{l,i+1} = \dfrac{A_{i+1/2}}{m_{v,i+1}S_{i+1}^0 + m_{l,i+1}} \left\{ -\left(P_{i+1}^{cl} - P_i^{cl}\right) + \left(L_{i+1}^{cl} - L_i^{cl}\right)\left(\dfrac{dP}{dL}\right)_{f,i+1/2} \right. \\ \qquad \left. + \left[\alpha_{i+1/2}\rho_{v,i+1/2} + \left(1-\alpha_{i+1/2}\right)\rho_{l,i+1/2}\right]\Omega^2 r_{i+1/2}^{cl} \cos\gamma_{i+1/2}^{cl}\left(L_{i+1}^{cl} - L_i^{cl}\right) \right\} \\ \qquad + \dfrac{m_{v,i}W_{v,i} + m_{l,i}W_{l,i}}{m_{v,i+1}S_{i+1}^0 + m_{l,i+1}} \\ W_{v,i+1} = S_{i+1}^0 W_{l,i+1} \end{cases} \tag{C.2}$$

8. Derive the corrected area A_{i+1}^* at node $i+1$ using Equation (C.3) and Z_{i+1} using Equation (C.4), where τ_z is the width ratio.

$$A_{i+1}^* = \frac{m/B_N}{\alpha_{i+1}\rho_{v,i+1}W_{v,i+1} + \left(1-\alpha_{i+1}\right)\rho_{l,i+1}W_{l,i+1}} \tag{C.3}$$

$$Z_{i+1} = \tau_z \sqrt{A_{i+1}^*} \tag{C.4}$$

9. Check the area error and use the corrected area A_{i+1}^* to iterate until the required tolerance is reached.
10. Derive the vapour relative velocity $W_{v,i+1}^*$ at node i+1 using Equation (19). Derive the corrected slip ratio S_{i+1}^* and iterate until the required tolerance is reached.
11. Derive the liquid enthalpy $H_{l,i+1}$ at node $i+1$ using Equation (C.5).

$$\begin{aligned} H_{l,i+1} = \frac{1}{\left(1-\alpha_{i+1}\right)A_{i+1}\rho_{l,i+1}W_{l,i+1}} \Bigg[& -W_{f,i+1/2}\left(L_{i+1}^{cl} - L_i^{cl}\right) \\ & + \alpha_i A_i \rho_{v,i} W_{v,i}\left(H_{v,i} + \frac{W_{v,i}^2 - U_i^2}{2}\right) + \left(1-\alpha_i\right)A_i\rho_{l,i}W_{l,i}\left(H_{l,i} + \frac{W_{l,i}^2 - U_i^2}{2}\right) \\ & - \alpha_{i+1}A_{i+1}\rho_{v,i+1}W_{v,i+1}\left(H_{v,i+1} + \frac{W_{v,i+1}^2 - U_{i+1}^2}{2}\right) - \frac{W_{l,i+1}^2 - U_{i+1}^2}{2} \Bigg] \end{aligned} \tag{C.5}$$

12. Derive the corrected liquid temperature $T_{l,i+1}^*$ at node $i+1$ using Equation (C.6).

$$T_{l,i+1}^* = T_{l,i} + \frac{H_{l,i+1} - H_{l,i}}{Cp_{l,i+1/2}} \tag{C.6}$$

13. Check the liquid temperature error and iterate until the required tolerance is reached.
14. Derive the geometrical information of PL and SL using Equation (C.7).

$$\begin{cases} x_{i+1}^{pl} = x_{i+1}^{cl} + \dfrac{Z_{i+1}}{2}\cos\left(\beta_{i+1} - \dfrac{\pi}{2}\right) \\ y_{i+1}^{pl} = y_{i+1}^{cl} + \dfrac{Z_{i+1}}{2}\sin\left(\beta_{i+1} - \dfrac{\pi}{2}\right) \\ x_{i+1}^{sl} = x_{i+1}^{cl} - \dfrac{Z_{i+1}}{2}\cos\left(\beta_{i+1} - \dfrac{\pi}{2}\right) \\ y_{i+1}^{sl} = y_{i+1}^{cl} - \dfrac{Z_{i+1}}{2}\sin\left(\beta_{i+1} - \dfrac{\pi}{2}\right) \end{cases} \tag{C.7}$$

15. Loop i from 1 to $n_{mfp} - 1$.

Author Contributions

H.L. mainly contributes in methodology, investigation, CFD, flow analysis and original draft preparation; S.R. mainly contributes in mathematical models, model parameters and validation of CFD, flow analysis and draft review; Z.Y. mainly contributes in conceptualization, draft review and editing, project administration and funding acquisition; G.Y. mainly contribute in providing appropriate design parameters of the turbine. All authors have read and agreed to the published version of the manuscript.

Conflicts of Interest

The authors declare that they have no known competing financial interests or personal relationships that could have appeared to influence the work reported in this paper.

Reference

[1] A.L. Austin, G.H. Higgins, J.H. Howard, The total flow concept for recovery of energy from geothermal hot brine deposits, University of California, Livermore, California, 1973. file://catalog.hathitrust.org/Record/102564884.

[2] T. Bond, Replacement of Joule-Thomson valves by two-phase flow turbines in industrial refrigeration applications, in: Proceedings, IMechE Conf. Trans., Mechanical Enginnering Publications, London, 1999: pp. 361–374.

[3] S.-Y. Cho, C.-H. Cho, C. Kim, Performance characteristics of a turbo expander substituted for expansion valve on air-conditioner, Exp. Therm. Fluid Sci. 32 (2008) 1655–1665. https://doi.org/10.1016/j.expthermflusci.2008.05.007.

[4] H. Li, W. Li, X. Zhang, Y. Zhu, Z. Zuo, H. Chen, Design method of a two-phase annular nozzle in cryogenic liquid expander, Proc. Inst. Mech. Eng. Part A J. Power Energy. 233 (2019) 762–772. https://doi.org/10.1177/0957650918822943.

[5] E.S. Starkman, V.E. Schrock, K.F. Neusen, D.J. Maneely, Expansion of a Very Low Quality Two-Phase Fluid Through a Convergent-Divergent Nozzle, J. Basic Eng. 86 (1964) 247–254. https://doi.org/10.1115/1.3653047.

[6] R.A. Brown, Flashing Expansion of Water Through a Converging-Diverging Nozzle, University of California, Berkeley, 1961. https://www.osti.gov/biblio/4793205. (accessed 20.06.14)

[7] K.F. Neusen, Optimizing of Flow Parameters for the Expansion of Very Low-Quality Steam, University of California, 1962. https://www.osti.gov/biblio/4784102. (accessed 20.06.14)

[8] D.J. Maneely, A Study of the Expansion Process of Low-Quality Steam through a de Laval Nozzle, University of California, Berkeley, 1962. https://www.osti.gov/biblio/4793611.

[9] A.L. Austin, A.W. Lundberg, Comparison of methods for electric power generation from geothermal hot water deposits, ASME Paper No. 74-WA, 1974. https://www.osti.gov/biblio/5067175. (accessed 20.06.14)

[10] T.W. Alger, Performance of two-phase nozzles for total flow geothermal impulse turbines, in: Proc. Second United Nations Symp. Dev. Use Geotherm. Resour., California Univ., Livermore (USA). Lawrence Livermore Lab., San Francisco, 1975. https://www.osti.gov/servlets/purl/5113781.

[11] W.J. Comfort III, Performance of a total-flow impulse turbine for geothermal applications, in: Twelfth Ersociety Energy Convers. Eng. Conf., La Grance, Illinois: American Nuclear Society., Washington, D.C., 1977: pp. 893–898.

[12] W.J. Comfort III, The design and evaluation of a two-phase turbine for low quality steam-water mixtures, University of California, 1977.

[13] W.J. Comfort III, C.W. Beadle, Design considerations for a two-phase turbine, in: San Francisco, California, 1978.

[14] D.G. Elliot, Theory and tests of two-phase turbines, Jet Propulsion Laboratory, 1982. https://doi.org/10.2172/5346135.

[15] L.G. Hays, J.J. Brasz, Two-phase turbines for compressor energy recovery, in: Proc. 1996 Int. Compress. Eng. Conf. Purdue Univ., Purdue University, West Lafayette, IN, United States, 1996.

[16] L.G. Hays, J.J. Brasz, Two-Phase-Flow Turbines as Stand-Alone Throttle Replacement Units in Large 2000-5000 Ton Centrifugal Chiller Installations, in: Proc. 1998 Int. Compress. Eng. Conf. Purdue, Purdue University, West Lafayette, IN, United States, 1998: pp. 792–802.

[17] J.J. Brasz, Performance characteristics of two-phase-flow turbo-expanders used in water cooled chillers, in: Proc. IMechE Int. Conf. Compressors Their Syst., Mechanical Enginnering Publications, London, 1999: pp. 171–182.

[18] T. He, C. Xia, Y. Zhao, L. Li, P. Shu, An experimental study on energy recovery by a pelton-type expander in a domestic refrigeration system, HVAC&R Res. 15 (2009) 785–799.

[19] Y. Beucher, E.V. Ksayer, D. Clodic, Characterization of friction loss in Pelton turbine, in: Proceeding 13th Int. Refrig. Air Cond. Conf. Purdue, Purdue University, West Lafayette, IN, United States, 2010: p. 1077.

[20] Y. Aaraj, S. Mortada, D. Clodic, M. Nemer, Design Of A Turgo Two-Phase Turbine Runner, in: Proceeding 15th Int. Refrig. Air Cond. Conf. Purdue, Purdue University, West Lafayette, IN, United States, 2014.

[21] L.G. Hays, D.G. Elliott, Two-phase engine, 3,879,949, 1975.

[22] W. Studhalter, D. Cerini, L. Hays, Demonstration of an advanced biphase turbine at Coso Hot Springs, Geothermal Resources Council, Davis, CA, United States, 1995.

[23] Z. Zhang, M. Li, Y. Ma, X. Gong, Experimental investigation on a turbo expander substituted for throttle valve in the subcritical refrigeration system, Energy. 79 (2015) 195–202. https://doi.org/10.1016/j.energy.2014.11.007.

[24] K. Akagawa, T. Fujii, S. Takagi, M. Takeda, K. Tsuji, Performance of Hero's Turbine Using Two-phase Mixture as Working Fluid: Experimental Results in an Air-water Two-phase System,

Bull. JSME. 27 (1984) 2795–2802.

[25] K. Akagawa, T. Fujii, J. Ohta, K. Inoue, K. Taniguchi, Performance characteristics of divergent-convergent nozzles for subcooled hot water, JSME Int. Journal. Ser. 2, Fluids Eng. Heat Transf. Power, Combust. Thermophys. Prop. 31 (1988) 718–726.

[26] J. Ohta, T. Fujii, K. Akagawa, N. Takenaka, Performance and flow characteristics of nozzles for initially subcooled hot water (influence of turbulence and decompression rate), Int. J. Multiph. Flow. 19 (1993) 125–136. https://doi.org/10.1016/0301-9322(93)90028-S.

[27] T. Fujii, J. Ohta, K. Akagawa, T. Nakamura, H. Asano, Performance characteristics of Hero's turbine using hot water as a working fluid, JSME Int. Journal. Ser. 2, Fluids Eng. Heat Transf. Power, Combust. Thermophys. Prop. 35 (1992) 319–324.

[28] Y. Zhao, A. Akbarzadeh, J. Andrews, Simultaneous desalination and power generation using solar energy, Renew. Energy. 34 (2009) 401–408. https://doi.org/10.1016/j.renene.2008.05.018.

[29] A. Date, S. Vahaji, J. Andrews, A. Akbarzadeh, Experimental performance of a rotating two-phase reaction turbine, Appl. Therm. Eng. 76 (2015) 475–483. https://doi.org/10.1016/j.applthermaleng.2014.11.039.

[30] G. Fabris, Two-phase reaction turbine, United States Patent 5,236,349, 1993. https://patents.google.com/patent/US5236349A/en. (accessed 20.06.14)

[31] S. Rane, L. He, Two-Phase Flow Analysis and Design of Geothermal Energy Turbine, in: IOP Conf. Ser. Mater. Sci. Eng., IOP Publishing, 2019: p. 12043.

[32] S. Rane, L. He, CFD analysis of flashing flow in two-phase geothermal turbine design, J. Comput. Des. Eng. 7 (2020) 238–250. https://doi.org/10.1093/jcde/qwaa020.

[33] S. Rane, L. He, Modelling of flash boiling in two phase geothermal turbine, in: Proc. 16th UK Heat Transf. Conf., Nottingham, United Kindom, 2019: p. 005.

[34] S. Rane, L. He, H. Ma, CFD modelling and analysis of Two-Phase Geothermal Energy Turbine in Project Combi-Gen, in: Int Conf Innov. Appl. Energy, Oxford, 2019: p. 257. https://doi.org/10.1093/jcde/qwaa020.

[35] N. Abuaf, B.J.C. Wu, G.A. Zimmer, P. Saha, Study of nonequilibrium flashing of water in a converging-diverging nozzle. Volume 1: experimental, Brookhaven National Lab., Upton, New York, United States, 1981.

[36] B.J.C. Wu, N. Abuaf, P. Saha, Study of nonequilibrium flashing of water in a converging-diverging nozzle. Volume 2. Modeling, Brookhaven National Lab., Upton, New York, United States, 1981.

[37] D.G. Elliott, E. Weinberg, Acceleration of liquids in two phase nozzles, Pasadena, Californica, United States, 1968. https://ntrs.nasa.gov/search.jsp?R=19680017730. (accessed 20.06.14)

[38] G.B. Wallis, One-dimensional two-phase flow, McGraw-Hill, New York, 1969.

[39] L. Cheng, Frontiers and Progress in Multiphase Flow I, Springer, Switzerland, 2014. https://doi.org/10.1007/978-3-319-04358-6.

[40] E.M. Greitzer, C.S. Tan, M.B. Graf, Internal flow: concepts and applications, Cambridge University Press, Cambridge, 2007.

[41] Y. Liao, D. Lucas, Computational modelling of flash boiling flows: A literature survey, Int. J. Heat Mass Transf. 111 (2017) 246–265. https://doi.org/10.1016/j.ijheatmasstransfer.2017.03.121.

[42] T. Zervogiannis, D.I. Papadimitriou, K.C. Giannakoglou, Total pressure losses minimization in turbomachinery cascades using the exact Hessian, Comput. Methods Appl. Mech. Eng. 199 (2010) 2697–2708. https://doi.org/https://doi.org/10.1016/j.cma.2010.05.014.

[43] V.K. Garg, Throughflow analysis of axial flow turbines, Comput. Methods Appl. Mech. Eng. 37 (1983) 129–137. https://doi.org/https://doi.org/10.1016/0045-7825(83)90116-0.

[44] W.H. Lee, A pressure iteration scheme for two-phase flow modeling, Los Alamos, New Mexico, United States, 1979. https://doi.org/10.1142/9789814460286_0004.

[45] A.K. Singhal, M.M. Athavale, H. Li, Y. Jiang, Mathematical basis and validation of the full cavitation model, J. Fluids Eng. 124 (2002) 617–624. https://doi.org/10.1115/1.1486223.

[46] P.J. Zwart, A.G. Gerber, T. Belamri, A two-phase flow model for predicting cavitation dynamics, in: ICMF 2004 Int. Conf. Multiph. Flow, Yokohama, Japan, 2004.

[47] N. Kurul, On the modeling of multidimensional effects in boiling channels, in: Proc. 27th Natl. Heat Transf. Conf., Minneapolis, Minnesota, United States, 1991.

[48] T.S. Shin, O.C. Jones, Nucleation and flashing in nozzles—1. A distributed nucleation model, Int. J. Multiph. Flow. 19 (1993) 943–964. https://doi.org/10.1016/0301-9322(93)90071-2.

[49] V.N. Blinkov, O.C. Jones, B.I. Nigmatulin, Nucleation and flashing in nozzles—2. Comparison with experiments using a five-equation model for vapor void development, Int. J. Multiph. Flow. 19 (1993) 965–986. https://doi.org/10.1016/0301-9322(93)90072-3.

[50] I.K. Karathanassis, P. Koukouvinis, M. Gavaises, Comparative evaluation of phase-change mechanisms for the prediction of flashing flows, Int. J. Multiph. Flow. 95 (2017) 257–270. https://doi.org/https://doi.org/10.1016/j.ijmultiphaseflow.2017.06.006.

[51] Q. Dang Le, R. Mereu, G. Besagni, V. Dossena, F. Inzoli, Computational Fluid Dynamics Modeling of Flashing Flow in Convergent-Divergent Nozzle, J. Fluids Eng. 140 (2018). https://doi.org/10.1115/1.4039908.

[52] W. Angielczyk, J.M. Seynhaeve, J. Gagan, Y. Bartosiewicz, D. Butrymowicz, Prediction of critical mass rate of flashing carbon dioxide flow in convergent-divergent nozzle, Chem. Eng. Process. - Process Intensif. 143 (2019) 107599. https://doi.org/https://doi.org/10.1016/j.cep.2019.107599.

[53] J.W. Gärtner, A. Kronenburg, A. Rees, J. Sender, M. Oschwald, G. Lamanna, Numerical and experimental analysis of flashing cryogenic nitrogen, Int. J. Multiph. Flow. 130 (2020) 103360. https://doi.org/https://doi.org/10.1016/j.ijmultiphaseflow.2020.103360.

[54] J. Zhu, S. Elbel, CFD simulation of vortex flashing R134a flow expanded through convergent-divergent nozzles, Int. J. Refrig. 112 (2020) 56–68. https://doi.org/https://doi.org/10.1016/j.ijrefrig.2019.12.005.

[55] J. Zhu, S. Elbel, Measurement of static pressure profiles of vortex flashing R134a flow expanded through convergent–divergent nozzles, Int. J. Refrig. 108 (2019) 258–270. https://doi.org/https://doi.org/10.1016/j.ijrefrig.2019.08.023.

[56] S. Yin, N. Wang, H. Wang, Nucleation and flashing inception in flashing flows: A review and model comparison, Int. J. Heat Mass Transf. 146 (2020) 118898. https://doi.org/https://doi.org/10.1016/j.ijheatmasstransfer.2019.118898.

[57] Y. Liao, D. Lucas, A review on numerical modelling of flashing flow with application to nuclear safety analysis, Appl. Therm. Eng. 182 (2021) 116002. https://doi.org/https://doi.org/10.1016/j.applthermaleng.2020.116002.

[58] K. Wolfert, The simulation of blowdown processes with consideration of thermodynamic nonequilibrium phenomena, in: Proc. Spec. Meet. Transient Two-Phase Flow, OECD/Nuclear Energy Agency, Toronto, Ontario, Canada, 1976: pp. 3–4.

[59] R.W. Lockhart, R.C. Martinelli, Proposed correlation of data for isothermal two-phase, two-

component flow in pipes, Chem. Eng. Prog. 45 (1949) 39–48.

[60] M.A. Woldesemayat, A.J. Ghajar, Comparison of void fraction correlations for different flow patterns in horizontal and upward inclined pipes, Int. J. Multiph. Flow. 33 (2007) 347–370. https://doi.org/10.1016/j.ijmultiphaseflow.2006.09.004.